Mid-Holocene climate at mid-latitudes: assessing the impact of the Saharan greening

Marco Gaetani[1], Gabriele Messori[2,3,4], Francesco S.R. Pausata[5], Shivangi Tiwari[5], M. Carmen Alvarez Castro[6], Qiong Zhang[7]

[1]University School for Advanced Studies IUSS, Pavia, Italy

[2]Dept. of Earth Sciences, Uppsala University, Uppsala, Sweden

[3]Swedish Centre for Impacts of Climate Extremes (climes), Uppsala University, Uppsala, Sweden

[4]Dept. of Meteorology and Bolin Centre for Climate Research, Stockholm University, Stockholm, Sweden

[5]Centre ESCER (Etude et la Simulation du Climat a; l'Echelle Regionale) and GEOTOP (Research Center on the Dynamics of the Earth System), Department of Earth and Atmospheric Sciences, University of Quebec in Montreal, Montreal, QC, Canada

[6]Dept. of Physical, Chemical and Natural Systems, Pablo de Olavide University, Seville, Spain.

[7]Department of Physical Geography and Bolin Centre for Climate Research, Stockholm University, Stockholm, Sweden

Correspondence to: Marco Gaetani (marco.gaetani@iusspavia.it)

Abstract. During the first half of the Holocene (11,000 to 5,000 years ago) the Northern Hemisphere experienced a strengthening of the monsoonal regime, with climate reconstructions robustly suggesting a greening of the Sahara region. Paleoclimate archives also show that this so-called African Humid Period (AHP) was accompanied by changes in the climate conditions at mid to high latitudes. However, inconsistencies still exist in reconstructions of the mid-Holocene (MH) climate at mid-latitudes, and model simulations provide limited support to reduce these discrepancies. In this paper, a set of simulations performed with a climate model is used to investigate the hitherto unexplored impact of the Saharan greening on mid-latitude atmospheric circulation during the MH. Numerical simulations show a year-round impact of the Saharan greening on the main circulation features in the Northern Hemisphere, especially during boreal summer when the African monsoon develops. Key findings include a westward shift of the global Walker Circulation, leading to a modification of the North Atlantic jet stream in summer and the North Pacific jet stream in winter. Furthermore, the Saharan greening modifies the atmospheric synoptic circulation over the North Atlantic, enhancing the effect of the orbital forcing on the transition of the North Atlantic Oscillation phase from prevailingly positive to negative in winter and summer. Although the prescription of vegetation in the Sahara does not improve the proxy-model agreement, this study provides a first constraint on the Saharan greening influence on northern mid-latitudes, opening new opportunities for understanding the MH climate anomalies in regions such as North America and Eurasia.

1 Introduction

The early and middle Holocene (11,000 to 5,000 years ago) were characterised by the summer solstice occurring close to the perihelion of the Earth's orbit, which led to increased insolation during boreal summer and consequent modifications in climate seasonality. This period is often referred to as the "Holocene thermal optimum" that resulted in remarkable climate and environmental changes in the Tropics and at mid and high latitudes. The Northern Hemisphere experienced a reinforcement of the global monsoonal regime (Bosmans et al., 2012; Haug et al., 2001; Jiang et al., 2015; Wang et al., 2008; Wu and Tsai, 2021; Yuan et al., 2004; Zhao and Harrison, 2012). This monsoonal intensification particularly manifested in Africa, leading to the so-called "African Humid Period" (AHP) and the subsequent greening of the Sahara (Adkins et al., 2006; Claussen et al., 1999, 2017; Claussen and Gayler, 1997; Hoelzmann et al., 1998; Larrasoaña et al., 2013; Pausata et al., 2020; Tierney et al., 2011, 2017; Tierney and DeMenocal, 2013).

At mid-latitudes, paleoclimate proxies suggest a complex climatic evolution: gradual cooling of the northeast Atlantic, contrasted with a warming in the western subtropical Atlantic, the eastern Mediterranean and the northern Red Sea from the early to the middle Holocene (Andersson et al., 2010; Rimbu et al., 2003). These changes were accompanied by prevailing negative phases of the Arctic and North Atlantic Oscillations (AO and NAO, respectively) (Nesje et al., 2001; Olsen et al., 2012; Rimbu et al., 2003). The proxy records further indicate region-specific climatic deviations from the pre-industrial climate: eastern North America and Scandinavia likely experienced warmer and drier; Western Europe, colder winters and warmer summers; Central Europe, an overall warming; the Mediterranean, colder and rainier conditions; and central Asia, increased annual rainfall, warmer winters and colder summers **(Fig. 1)** (see e.g., Cronin et al., 2005; Bartlein et al., 2011; Scholz et al., 2012; Samartin et al., 2017; Davis et al., 2003). However, the interpretation of these climatic changes, particularly on temperature and precipitation patterns, as indicated by proxies, seem potentially inconsistent with the suggested changes in the atmospheric circulation (e.g., a drier eastern North America, warmer Scandinavia and colder Mediterranean would be inconsistent with a positive-to-negative shift in the NAO/AO phase). Furthermore, differences exist in the estimation of both timing and magnitude of the Holocene thermal maximum at mid to high latitudes (Cartapanis et al., 2022; Kaufman et al., 2004; Renssen et al., 2009).
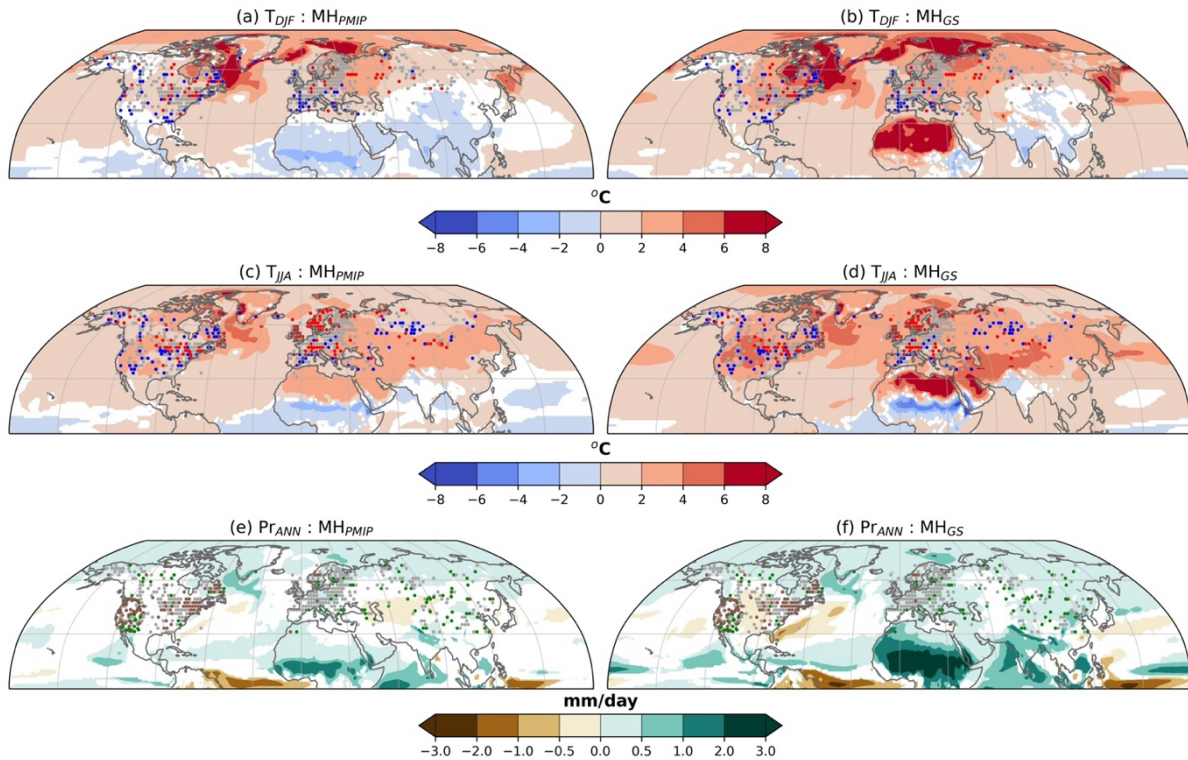
Figure 1. Model vs. proxy reconstruction comparison: Changes in (a, b) winter temperature, (c, d) summer temperature, and (e, f) annual precipitation between MH$_{PMIP}$ and PI (left) and between MH$_{GS}$ and PI (right). Coloured shading shows anomalies significant at the 95% confidence level after the Student's *t*-test. Filled dots show proxy sites and their MH signature relative to the PI. Red dots indicate warmer signature, blue dots indicate cooler signature, brown dots indicate drier signature, green dots indicate wetter signature, while grey dots indicate no change or inconclusive signature. Model simulations and proxy reconstructions are described in section 2.

In this context, climate models struggle to constrain the climate conditions associated with the Holocene thermal optimum. In the northern monsoon regions, precipitation increase is generally underestimated, while summer warming at mid to high latitudes is overestimated (Bartlein et al., 2017; Harrison et al., 2014). To explain the limitations of climate models in representing the middle Holocene climate, several studies pointed to the role of the vegetation together with other feedbacks at tropical and higher latitudes in modulating the climate response to the orbital forcing (Chandan and Peltier, 2020; Pausata et al., 2016; Swann et al., 2012, 2014). In particular, the remarkable greening of the Sahara influenced the regional and global climate during the middle Holocene. Modelling studies demonstrate that the resulting reduction in albedo and dust emission, along with enhanced water recycling associated with the increased vegetation cover, were key ingredients in maintaining the

intensified African monsoon regime during the AHP (Gaetani et al., 2017; Messori et al., 2019; Pausata et al., 2016; Tierney et al., 2017), as well as in reinforcing the global monsoon system, and modifying the tropical cyclone activity and the El Niño/Southern Oscillation variability (Pausata et al., 2017b, a; Piao et al., 2020; Sun et al., 2019; Swann et al., 2014). However, while paleoclimate modelling of the Green Sahara mainly focused on the impact in the Tropics and sub-tropics, the studies on climate responses at mid-latitudes is still limited.

The objective of this paper is to study the impact of the Saharan greening on the Northern Hemispheric mid-latitude atmospheric circulation and associated climate variability during the middle Holocene (MH). To achieve this, climate model is used to investigate the relevant underlying mechanisms. Moreover, the model-proxy agreement at mid-latitudes when considering vegetated Sahara with reduced dust emission is evaluated. This study focuses on the analysis of the winter (December to February, DJF) and summer (June to August, JJA) seasons in the Northern Hemisphere.

2 Data and methods

In this paper, the climate experiments described in Pausata et al. (2016) are analysed. These simulations were conducted using version 3.1 of the atmosphere–ocean coupled climate model EC-Earth (Hazeleger et al., 2010). The atmospheric model is based on the Integrated Forecast System (IFS cycle 36r4) (https://www.ecmwf.int/en/forecasts/documentation-and-support), including the H-TESSEL land model (van den Hurk et al., 2000). The simulations are run at T159 horizontal spectral resolution (~1.125°, approximately 125 km) with 62 vertical levels. The atmospheric component is coupled by the OASIS 3 coupler (Valcke 2006) to the Nucleus for European Modeling of the Ocean (NEMO) version 2 (Madec 2008), and the Louvain-la-Neuve Sea Ice Model version 3 (LIM3) (Vancoppenolle et al., 2009). The ocean component NEMO has a nominal horizontal resolution of 1° and 46 vertical levels.

A 700-year pre-industrial (PI) control simulation following the CMIP5 protocol (Taylor et al., 2012) was conducted to provide initial conditions to the MH simulations, which were run for about 300 years (climate equilibrium is reached after 100–200 years, depending on the experiment). For each experiment, data from the last 30 years are retained for analysis. The atmospheric dust concentration representative of the PI conditions is prescribed in the PI simulation by using the long-term monthly mean (1980-2015) from the MERRAero product. This dataset includes the radiative coupling of the GEOS-5 climate model to the GOCART aerosol module and assimilates satellite retrievals of aerosol optical depth (AOD) from the MODIS sensor. Details on the MERRAero dataset are available at https://gmao.gsfc.nasa.gov/reanalysis/merra/MERRAero/. In the analysed simulations, the EC-Earth3.1 simulates the direct effect of dust on the atmospheric radiative balance, though it does not simulate indirect effect on cloud formation and microphysics.

A MH simulation is run following the PMIP3 protocol (MH$_{PMIP}$): the orbital forcing is set to MH values (6,000 years BP); the solar constant, land cover, ice sheets, topography, and coastlines are set to PI conditions, as well as the greenhouse gas concentrations, with the exception of the methane concentration set at 650 ppb. An additional MH simulation is run with

prescribing Green Sahara (GS) conditions, namely vegetated surface and reduced dust emission in the Sahara–Sahel region (MH$_{GS}$) (11°–33°N, 15W°– 35°E). Land cover in the Sahara is prescribed to be evergreen shrub with a leaf area index (LAI)

105 of 2.6. This modification in land surface type corresponds to a change of surface albedo from 0.30 (desert) to 0.15 (shrub). Surface roughness and soil wetness are prescribed to PI values. Dust emission typical of the AHP is simulated by prescribing an 80% reduction in dust concentration throughout the troposphere (up to 150 hPa) over a broad area around the Sahara region [see Fig. S1 in Gaetani et al. (2017)]. The inclusion of dust reduction in the experimental setup significantly influences the simulation of the monsoonal dynamics, leading to an increase of around 30% of cumulated precipitation compared to

110 simulations with prescribing vegetation only (see Pausata et al., 2016). A comparable effect of dust reduction has been observed in other modelling studies by Thompson et al. (2019), Hopcroft and Valdes (2019) and Sagoo and Storelvmo (2017), confirming the relevance and comparability of the model's response to dust effects. Although this experimental design is highly idealized, it is firmly grounded in paleoclimatic reconstructions for the MH from both dust (deMenocal et al., 2000; McGee et al., 2013) and pollen archives (Hély et al., 2014; Lézine et al., 2011). The experimental setup is summarized in

115 **Table 1**.

Table 1. Experimental set-up. Vegetation type, surface albedo and LAI refer to the Sahara region.

Simulation	Orbital forcing	GHGs	Vegetation type	Albedo	LAI	Dust concentration
PI	Present day	PI	Desert	0.30	0	1980-2015 climatology
MH$_{PMIP}$	6ka	MH	Desert	0.30	0	1980-2015 climatology
MH$_{GS}$	6ka	MH	Evergreen shrub	0.15	2.6	80% reduced

The climates in the MH$_{PMIP}$ and MH$_{GS}$ simulations are compared with multi-archival proxy reconstructions of continental

120 seasonal temperatures and annual precipitation. To this end, statistically significant anomalies (MH minus PI) simulated by the model are compared with MH signatures as indicated by a compilation of proxy records. This compilation not only builds upon datasets previously available from Bartlein et al. (2011) and Hermann et al. (2018) but also enriches it with 89 additional multi-archival, multi-proxy records, as listed in **Table A1**. To assess the agreement between proxy data and model simulations, the MH signatures at each proxy site are assigned to categories such as wetter/drier/no change or inconclusive and

125 warmer/cooler/no change or inconclusive. Proxy-model agreement is assessed using the weighted Cohen's Kappa index (κ), following DiNezio and Tierney (2013). The Cohen's Kappa index quantifies agreement between climate variables form climate simulations and proxy reconstructions through the probability that, at the proxy sites, the two data sets agree on the category of anomaly (e.g., positive/negative/no change in both simulation and proxy), but not by chance alone. The index is calculated by constructing a data matrix with the number of sites where the two data sets agree, partially disagree (one indicates a positive

or a negative anomaly, while the other indicates no change) and completely disagree (one indicates a positive anomaly while the other indicates a negative anomaly, or vice versa). This data matrix is then multiplied by a weight matrix, to penalise complete disagreement more than partial disagreement. The resultant values for the index range from 0 to 1, where 0 indicates no agreement, 0.5 indicates partial agreement, and 1 indicates perfect agreement. The Cohen's Kappa index is calculated separately over four regions: North America, Pacific Coast (180–100°W; 30–70°N); North America, Atlantic Coast (100–30°W, 30–70°N); Europe and Mediterranean (20°W–50 °E, 30–70°N); and Asia (50–180°E, 30–70°N) (Fig. A1).

Part of the analysis of atmospheric circulation variability focuses on the North Atlantic region, as in the present climate this relates to climate variability in both Eurasia and North America. The main modes of variability of the North Atlantic atmospheric circulation are extracted at the monthly and daily time scales, by applying a principal component analysis (PCA) (Wilks, 2019) to the geopotential height anomalies at 500 hPa over the domain (80W°– 30°E, 20°–80°N). In order to assess the modifications in the circulation patterns in the MH experiments relative to the PI simulation, all geopotential height anomalies are computed with respect to the PI climatology. The PCA is then applied to concatenated anomaly data from all three simulations. That is, the data matrix, Z, used to compute the covariance matrix, which is then used to find eigenvectors and eigenvalues (Wilks, 2019), is defined as: $Z = \begin{bmatrix} PI \\ MH_{PMIP} \\ MH_{GS} \end{bmatrix}$. Here PI, MH_{PMIP} and MH_{GS} are themselves matrices, with longitude and latitude data (55×30 grid points) arranged in columns and the time steps (30×3 or 30×92 for the monthly and daily analyses, respectively) arranged in rows.

The first EOF and the associated expansion coefficient time series derived from the PCA of the monthly anomalies are used to represent, respectively, the spatial pattern of the North Atlantic Oscillation (NAO) and its time evolution (NAO index, NAOI) as the NAO is acknowledged as the dominant mode of the atmospheric circulation in the North Atlantic region (Hurrell et al., 2003). At daily time scale, the first several PCA modes (first 7 modes in winter and first 8 modes in summer, accounting for 70% of the circulation variability) are used to classify the weather variability affecting North America, the North Atlantic and Europe. Because the selected EOFs show poor separation at the daily time scale, a rotation is applied (Wilks, 2019), and the rotated EOFs are used with a k-means classification algorithm (Wilks, 2019) to identify the four canonical weather regimes (WRs) characterising the synoptic atmospheric variability in the North Atlantic (Michelangeli *et al.*, 1995).

In order to facilitate the proxy-model comparison, all climate simulations are remapped to the 2-degree grid of the Bartlein et al. (2011) dataset, which is the only proxy dataset on a regular grid used in this study.

3 Results

3.1 Climate response to Saharan greening in the Northern Hemisphere

In this section, the DJF and JJA climatological responses of near-surface temperature, precipitation and atmospheric circulation to changes in both the MH orbital parameters alone, and in combination with prescribed Saharan greening, are shown. These

responses are quantified by comparing the differences between the MH_PMIP and MH_GS experiments against the PI simulation, respectively.

As a consequence of the change in the orbital parameters, the Northern Hemisphere displays a significantly warmer 2-m temperature in both seasons and experiments **(Fig. 1a-d and Fig. 2)**. The warming is significantly more pronounced when

165   Saharan greening is prescribed, in both winter and summer **(Fig. 1a-d and Fig. 2)**. In winter, the warming peaks in the Arctic region, presumably due to the loss of sea ice **(Fig. 1a, b)**. Moreover, in the MH_GS experiment, the reduced albedo associated with the vegetation cover increases the radiative forcing in the Saharan region, resulting in a warming effect in the northern tropics **(Fig. 1a, b and Fig. 2a)**. In summer, the Northern Hemisphere is homogeneously warmer from the polar regions to the subtropics **(Fig. 1c, d and Fig. 2b)**. The surface cooling associated with the intensification of the African monsoon is visible

170   in Northern Africa in both the experiments and is more pronounced in the MH_GS experiment **(Fig. 1c, d)** [see also Pausata et al. (2016); Gaetani et al. (2017)].
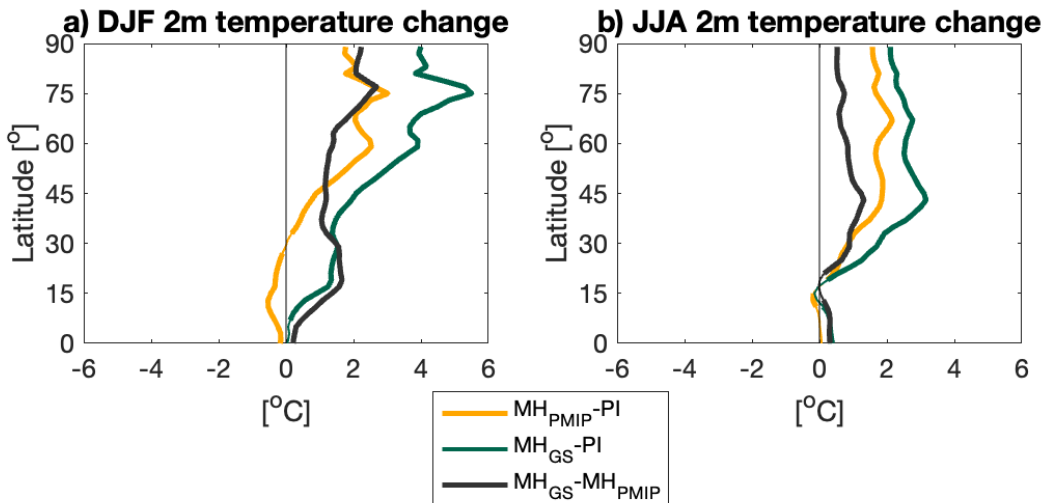
Figure 2. Climatological latitudinal mean changes in 2-m temperature in the MH_PMIP (yellow lines) and MH_GS (green lines)

175   **simulations relative to the PI simulation, and in the MH_GS simulation relative to the MH_PMIP simulation (black lines), in boreal (a) winter and (b) summer. Thicker lines display anomalies significant at the 95% confidence level after a Student's *t* test.**

Precipitation in the Northern Hemisphere mid to high latitudes shows a significant increase in winter and summer, in both the MH experiments, with a significant intensification when the Saharan greening is prescribed **(Fig. 1e, f and Fig. 3)**. This

180   precipitation response is associated with a slowing down of the westerly upper tropospheric flow in the subtropics, along with a reinforcement at mid-latitudes **(Fig. 4)**. The precipitation is also significantly enhanced in the northern Tropics for both the

MH experiments, with a vegetated Sahara again resulting in a further significant increase relative to MH$_{PMIP}$ **(Fig. 1e, f and Fig. 3)**. In particular, both MH experiments show an intensification of the boreal summer monsoonal regime, which is accompanied by a northward shift of the precipitation belt **(Fig. 1e, f and Fig. 3)**.

185
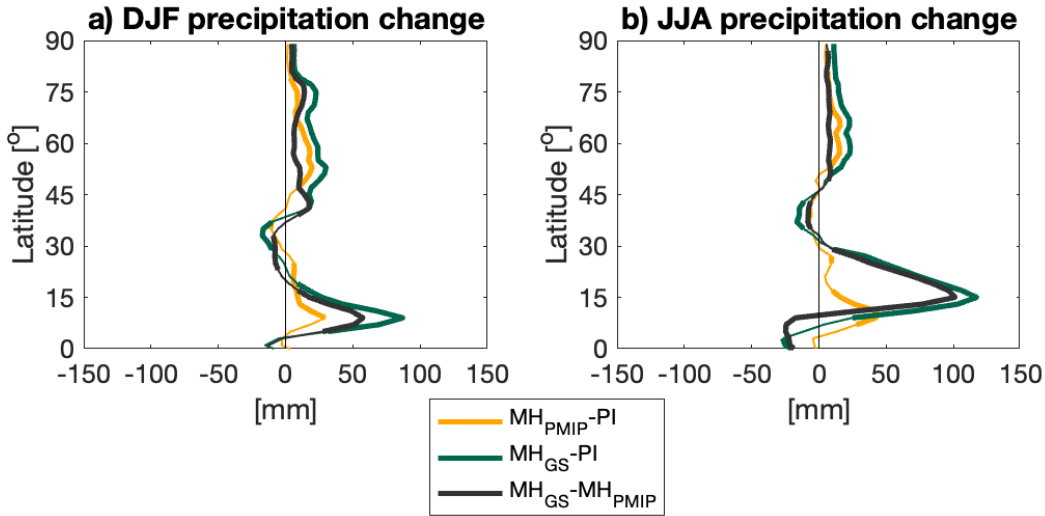
Figure 3. Climatological latitudinal mean changes in precipitation in the MH$_{PMIP}$ (yellow lines) and MH$_{GS}$ (green lines) simulations with respect to the PI simulation, and in the MH$_{GS}$ simulation with respect to the MH$_{PMIP}$ simulation (black lines), in boreal (a) winter and (b) summer. Thicker lines display anomalies significant at the 95% confidence level after a Student's *t* test.

190
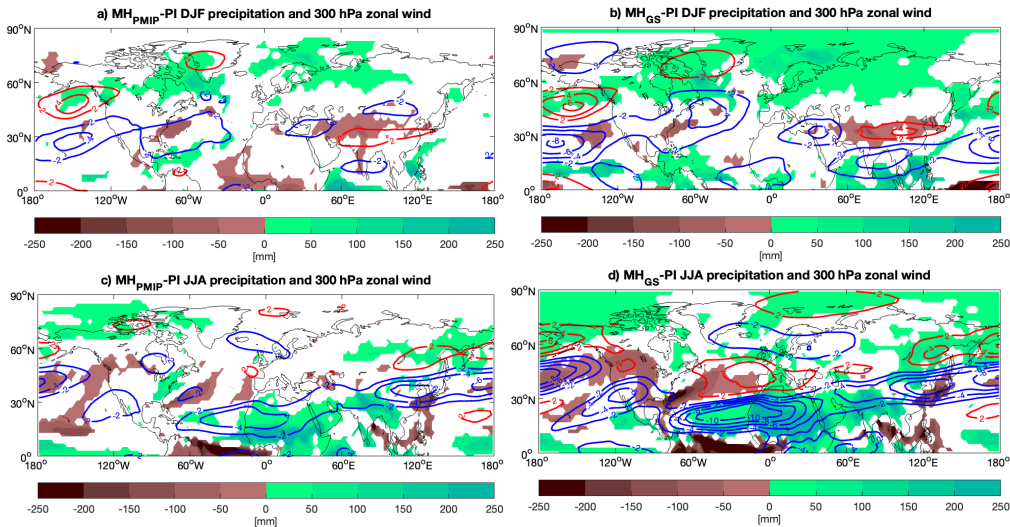
Figure 4. Changes in precipitation [mm day^{-1}] in the (a, c) MH$_{PMIP}$ and (b, d) MH$_{GS}$ simulations with respect to the PI simulation, in (a, b) winter and (c, d) summer. Only areas showing statistically significant precipitation anomalies, estimated by a Student's t-test at 95% confidence level, are shown. Red and blue contours show, respectively, positive and negative change in the zonal wind velocity at 300 hPa [m s^{-1}].

The winter precipitation response in the MH experiments is characterised by significant dry anomalies in central Asia and significant wet anomalies at high latitudes in North America and Eurasia, which are scattered in the MH$_{PMIP}$ simulation and widespread in the MH$_{GS}$ experiment **(Fig. 4a, b)**. The presence of vegetated Sahara also compensates the dry anomalies simulated in northern tropical Africa in the MH$_{PMIP}$ experiment **(Fig. 4a, b)**. The meridional profile of the westerly upper tropospheric flow to the west of the North American continent (corresponding to the end of the North Pacific storm track) shows an intensification and a zonalisation of the jet stream in both MH simulations with respect to the PI experiment **(Fig. 5a)**, suggesting a modification in the location and magnitude of the storm track affecting the North American west coast. In the North Atlantic, to the west of the Eurasian continent, both MH simulations show a slight weakening of the westerly wind at the mid-latitudes, accompanied by a slight intensification at the sub-polar latitudes **(Fig. 5b)**, suggesting a possible modification of the circulation pattern over the North Atlantic. However, the prescribed vegetation in the Sahara does not significantly influence the winter dynamics of the jet stream beyond the changes induced by the orbital parameters alone. At global scale, the dynamical signature of the MH experiments in winter is marked by a westward shift of the Walker circulation, as shown by the changes in the velocity potential and divergent wind in the upper troposphere **(Fig. 6a, b)**.

In summer, both MH experiments show wet anomalies in the monsoonal region, as well as the tropical North Atlantic and equatorial Pacific **(Fig. 4c, d)**. The response is stronger in the MH$_{GS}$ simulation due to the effect of Saharan greening on the African monsoon **(Fig. 4c, d)**. Moreover, in the MH$_{GS}$ experiment, a significant drying at subtropical latitudes is simulated in the North Pacific, North America and the North Atlantic **(Fig. 4d)**. The meridional profile of the westerly upper tropospheric flow shows significant changes in the MH$_{GS}$ simulation with respect to the PI and MH$_{PMIP}$ experiments. Specifically, to the west of the North American continent, there is a significant weakening of the mid-latitude westerlies, accompanied by an intensification at the sub-polar latitudes **(Fig. 5c)**. This suggests a northward shift in the jet stream and a modification in the location and intensity of the storm track affecting the North American west coast when Saharan greening is prescribed. To the west of the Eurasian continent, there is a significant reinforcement and southward shift of the subpolar jet stream **(Fig. 5d)**, indicating a shift in the location and magnitude of the North Atlantic storm track. Similar to the winter season, the global Walker circulation shows a westward shift in summer **(Fig. 6c, d)**. The MH$_{GS}$ experiment shows a stronger response, which could be expected, but also shows an atmospheric bridge in the upper troposphere, represented by the easterly divergent wind anomalies. This bridge connects a divergence anomaly in the Indian Ocean with a convergence anomaly in the tropical North Atlantic, as shown by the negative and positive velocity potential anomalies, respectively **(Fig. 6d)**. This feature is reflected

in the simulated merging of the mid-latitude and subtropical jet streams in the North Atlantic **(Fig. 5d and 4d)**, suggesting a potential mechanism connecting the reinforcement of the monsoonal regime with modifications of the mid-latitude circulation.
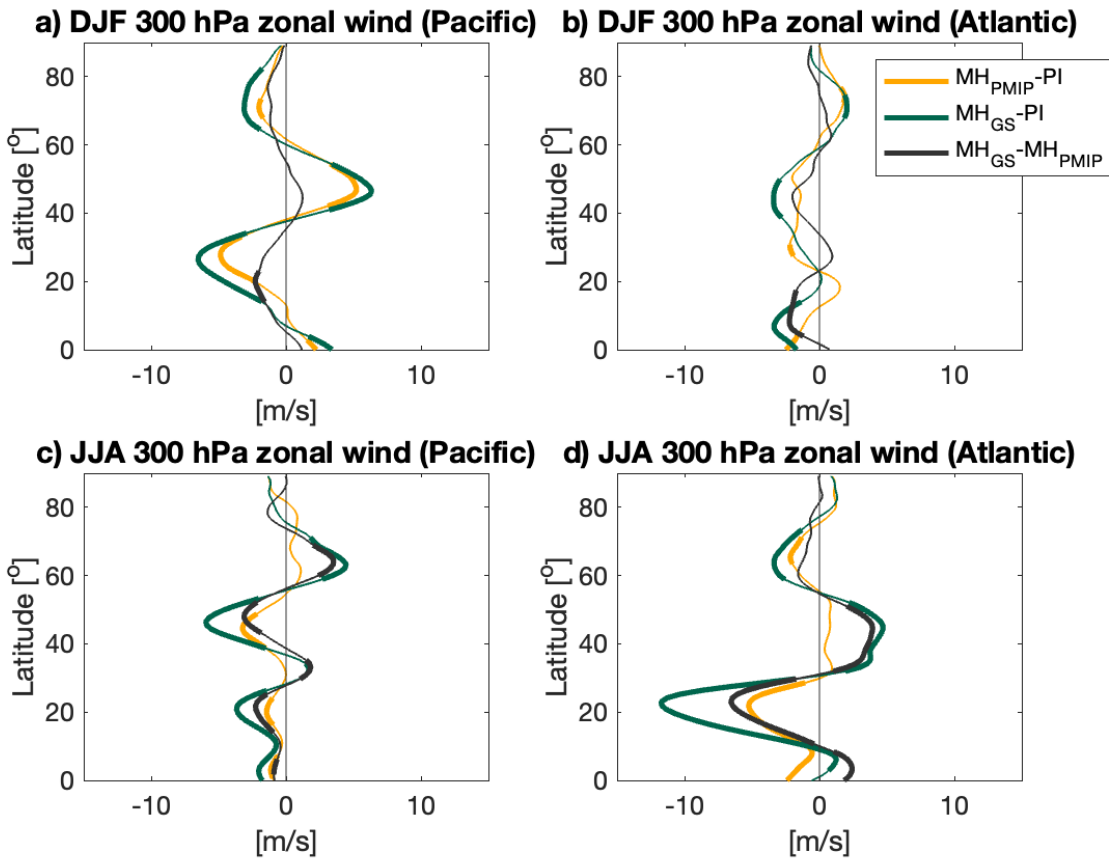
Figure 5. Climatological latitudinal mean changes in the zonal wind at 300 hPa in the MH$_{PMIP}$ (yellow lines) and MH$_{GS}$ (green lines) simulations with respect to the PI simulation, and in the MH$_{GS}$ simulation with respect to the MH$_{PMIP}$ simulation (black lines), at (a, c) 150°W (North Pacific) and (b, d) 30°W (North Atlantic), in boreal (a, b) winter and (c, d) summer. Thicker lines display anomalies significant at the 95% confidence level after a Student's t test.
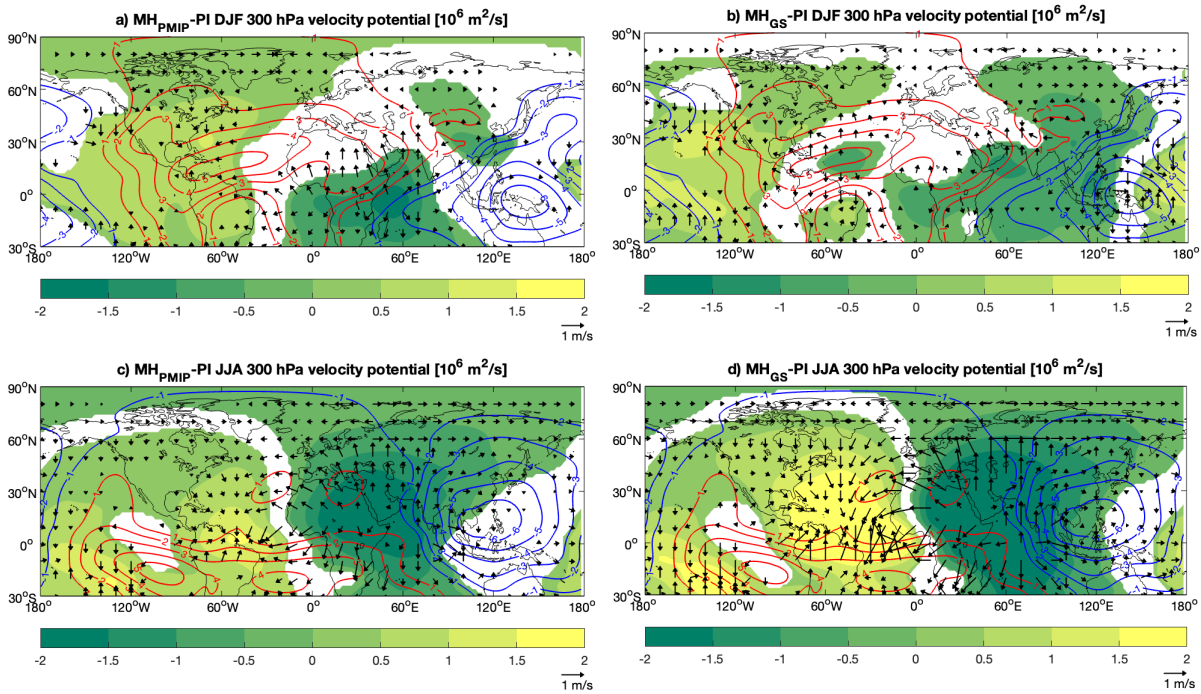
Figure 6. Changes in the velocity potential (shadings) and divergent wind at 300 hPa (vectors) in the MH$_{PMIP}$ and MH$_{GS}$ simulations in (a, b) DJF and (c, d) JJA with respect to the PI simulation. Red and blue contours display the climatological pattern of velocity potential in the PI simulation. Only locations and vectors showing statistically significant velocity potential and divergent wind anomalies, at the 95% level of confidence after a Student's *t* test, are shown.

3.2 Changes in the North Atlantic Oscillation

240   The NAO is the main mode of atmospheric variability influencing climate patterns in the North Atlantic, Europe, and North America (Ambaum et al., 2001; Chartrand and Pausata, 2020; Hurrell et al., 2003). In this section, the changes in NAO variability in the MH experiments with respect to the PI simulation are examined.

In winter, the NAO pattern identified in the model simulations reflects the canonical pattern described in the literature, with a strong meridional geopotential dipole in the North Atlantic explaining 28% of the total variability (Ambaum et al., 2001;
245   Hurrell et al., 2003) **(Fig. A2a)**. In the PI simulation, the NAOI is characterised by a distribution skewed towards positive values **(Fig. 7a)**. The NAO positive phase in the PI simulation is associated with warm anomalies in central and northern Europe and the east coast of North America, and cold anomalies in North Africa **(Fig. 8a)**. Moreover, this phase correlates with dry conditions in southern Europe and wetter conditions in Scandinavia **(Fig. 8b)**. Consistent with previous findings (e.g., Nesje et al., 2001; Rimbu et al., 2003; Olsen et al., 2012), changes in orbital parameters and the Saharan greening lead to a
250   shift of the NAOI phase towards negative values in MH$_{GS}$ **(Fig. 7a)**. A Kolmogorov-Smirnov test confirms that these shifts in

the NAOI distributions in both MH$_{PMIP}$ and MH$_{GS}$ experiments are statistically significant when compared to the PI simulation (p<0.02). However, the difference in the NAOI distributions between the MH$_{GS}$ and MH$_{PMIP}$ experiments is weakly significant (p<0.11). Circulation and surface anomaly patterns associated with the NAO positive phase in the MH$_{PMIP}$ (not shown) and the MH$_{GS}$ experiments **(Fig. 8c, d)** are very similar. The tendency towards a prevailing neutral-to-negative NAO phase in the MH

255   simulations is then expected to result in colder winters in central and northern Europe and eastern North America, and warmer conditions in northern Africa, along with wetter southern Europe and drier eastern North America and Scandinavia **(Fig. 8c, d)**. In particular, the thermal and rainfall anomalies are more pronounced when Saharan greening is taken into account, due to the larger difference in the NAO phase shift with respect to the PI period.
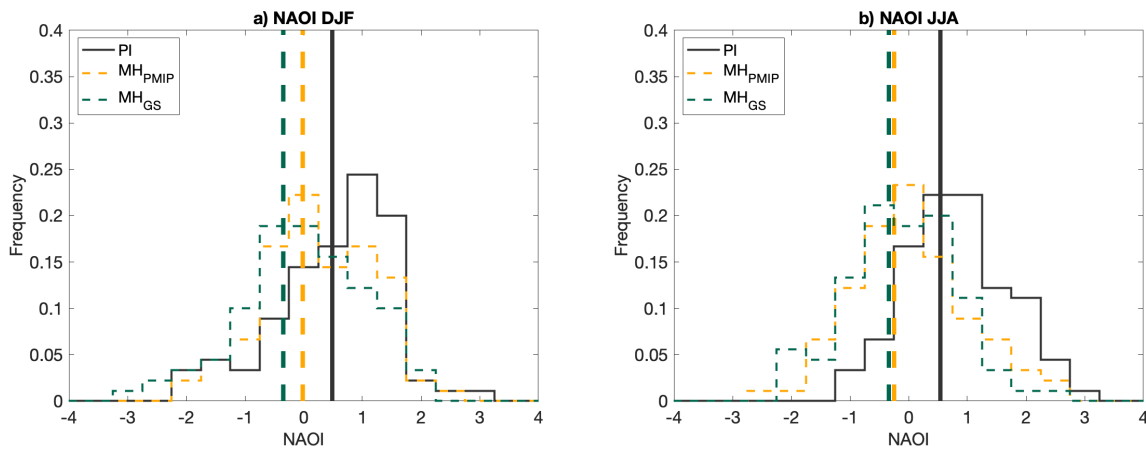
260

Figure 7. Distributions of the NAOI in the PI simulation (solid line), and in the MH$_{PMIP}$ and MH$_{GS}$ experiments (dashed lines), in (a) winter and (b) summer; the vertical lines indicate the medians of the distributions.
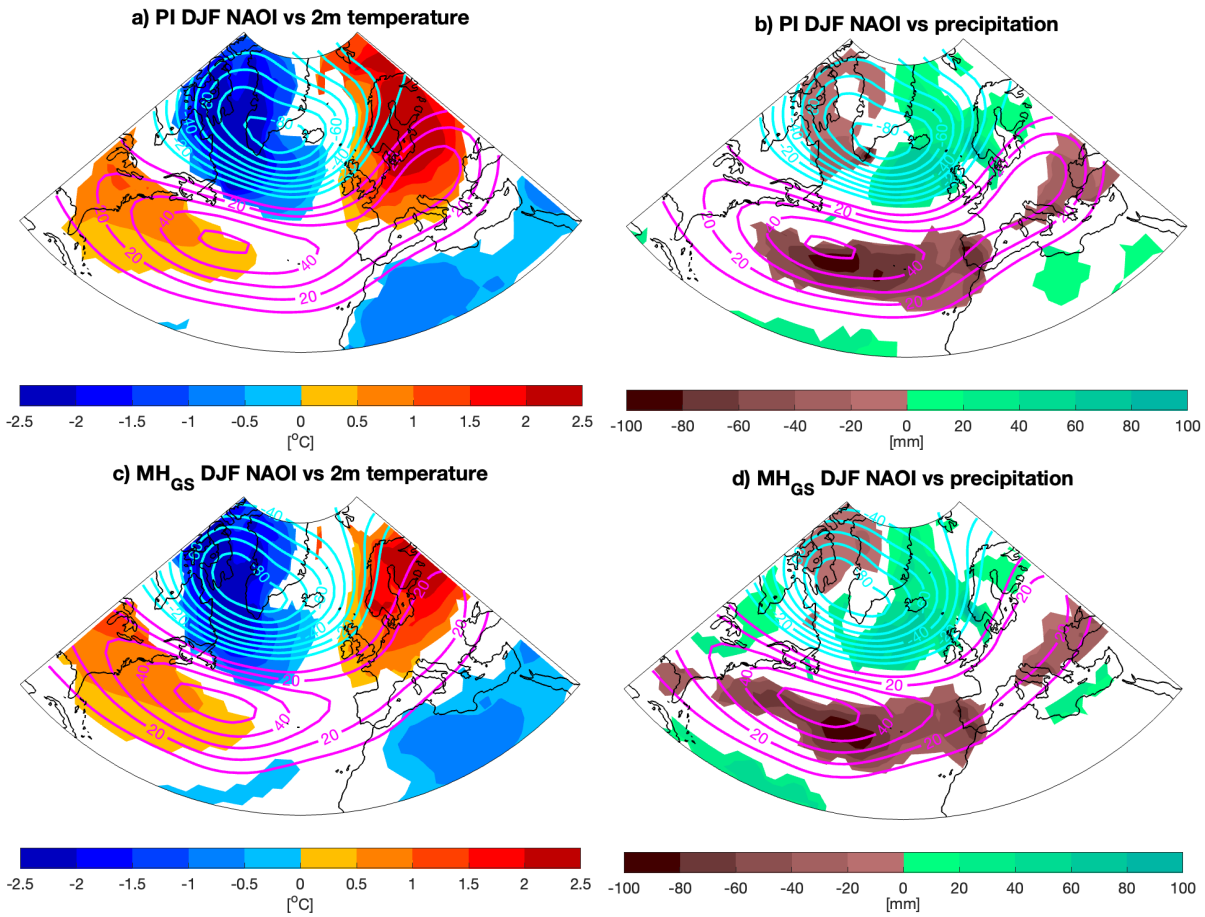
Figure 8. Winter NAO patterns (contours) and associated thermal and rainfall anomalies (shadings), obtained by regressing, respectively, geopotential height at 500 hPa [m], (a, c) 2-m temperature and (b, d) precipitation onto the NAOI in the (a, b) PI and (c, d) MH$_{GS}$ simulations. Only significant anomalies in 2-m temperature and precipitation are shown, assessed by using a Student's t test at 95% level of confidence.

In summer, the modelled NAO pattern reflects the canonical summer NAO pattern, characterised by weaker and less geographically extended anomalies than its winter counterpart, along with a northward shift of the meridional dipole (Bladé et al., 2012; Folland et al., 2009), explaining 23% of the total variability **(Fig. A2b)**. In the PI simulation, the NAOI is characterised by a prevailing positive phase **(Fig. 7b)**, associated with warm summers in western Europe and eastern North America and cold summers in the eastern Mediterranean and the North Atlantic, accompanied by dry conditions in northern Europe and wet conditions in the western Mediterranean **(Fig. 9a, b)**. The prevailing NAO phase turns negative when the orbital parameters are changed **(Fig. 7b)**. The phase shift is statistically significant in both the MH$_{PMIP}$ and MH$_{GS}$ experiments with respect to the PI simulation, as verified by a Kolmogorov-Smirnov test (p<0.01). However, it is noteworthy that the

Saharan greening effect does not introduce significant differences in this phase shift (p<0.49). A prevailing negative NAO phase then results in warmer summers in the eastern Mediterranean and northern Africa, and wetter summers in northern Europe **(Fig. 9c, d)**.
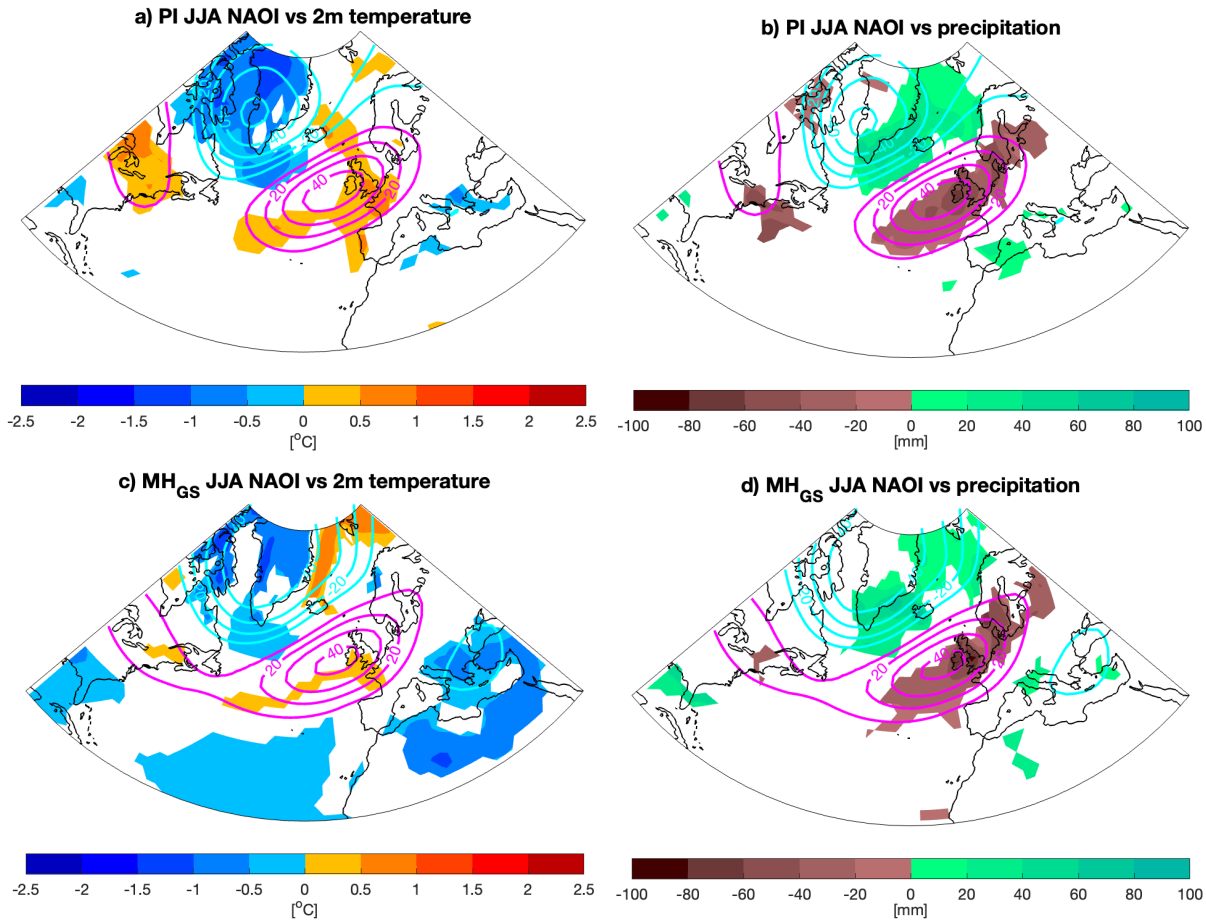
Figure 9. Summer NAO patterns (contours) and associated thermal and rainfall anomalies (shadings), obtained by regressing, respectively, geopotential height at 500 hPa [m], (a, c) 2-m temperature and (b, d) precipitation onto the NAOI in the (a, b) PI and (c, d) MH$_{GS}$ simulations. Only significant anomalies in 2-m temperature and precipitation are shown, assessed by using a Student's _t_ test at 95% confidence level.

3.3 North Atlantic Weather Regimes

The modifications in the atmospheric circulation variability over North America, the North Atlantic and Europe are explored at synoptic time scale through the analysis of the North Atlantic WRs (Hochman et al., 2021; Michelangeli et al., 1995) for the PI simulation and the MH experiments. Although year-round definitions of North Atlantic WRs exist (Grams et al., 2017; Hochman et al., 2021), they are often defined separately for the summer and winter seasons, and this is the approach adopted in this paper.

Model simulations show that the winter synoptic circulation is characterised by the four canonical WRs described in the literature (Cassou et al., 2004). The occurrences of these WRs are relatively uniform: two WRs are associated with the NAO's positive and negative phases (NAO+ and NAO-), accounting for approximately 50% of the analysed days. The remaining 50% are associated with a Scandinavian blocking (SB) or an Atlantic ridge (AR) pattern **(Table 2 and Fig. A3)**. It is highlighted that NAO+ and NAO-, as defined from the clustering of the daily variability, do not show the spatial symmetry typically associated with the NAO's positive and negative phases defined as the first EOF of the interannual variability (see **Fig. A2a and A3a, b**). Consistent with the analysis of the monthly NAO and previous research (Nesje et al., 2001; Rimbu et al., 2003; Olsen et al., 2012), the modification of the orbital parameters leads to a reduction in the occurrence of NAO+, which becomes residual in the MH$_{GS}$ experiment with respect to the PI simulation, along with an increase in the frequency of NAO- from PI to MH$_{GS}$ **(Table 2)**. However, the increase in NAO- does not fully offset the decrease in NAO+, resulting in increased AR and SB frequencies, with SB becoming the dominant WR (30.8%) in the MH$_{GS}$ experiment **(Table 2)**. The changes in the WR occurrence show a monotonic behaviour from the PI simulation to the MH experiments, with more pronounced changes observed in the MH$_{GS}$ experiment compared to MH$_{PMIP}$ **(Table 2)**, suggesting that the effect of the Saharan greening on the atmospheric circulation and the associated thermal and rainfall anomalies amplifies the changes driven solely by the orbital forcing. Therefore, the modifications in the WR dynamics are discussed in detail only for the MH$_{GS}$ experiment.

The NAO+ circulation pattern dominating the winter circulation in PI is associated with warm and wet anomalies in central and western Europe and southern Scandinavia, and cold and dry anomalies in North America and northern Scandinavia, along with dry anomalies in the eastern Mediterranean **(Fig. 10a and 11a)**. In the MH$_{GS}$ experiment, the large reduction in the occurrence of the NAO+ pattern is partially offset by the increased occurrence of NAO-, leading to cold anomalies in Scandinavia and eastern North America, paired with warm anomalies in polar North America, western Mediterranean and North Africa. It also results in wet anomalies over polar North America and central and eastern Europe, while dry anomalies in the Mediterranean **(Fig. 10d and Fig. 11d)**. The increased occurrence of SB in the MH$_{GS}$ experiment indicates reinforced cold anomalies in polar North America, Europe and the Mediterranean, and warm anomalies in northern Scandinavia and eastern North America, accompanied by dry anomalies in western and central-northern Europe and polar North America, and wet anomalies in the Mediterranean **(Fig. 10f and Fig. 11f)**.

320 **Table 2. WR occurrence in the PI and MH simulations, in percentage. The regimes are: NAO+, positive phase of the North Atlantic Oscillation; NAO-, negative phase of the North Atlantic Oscillation; AR, Atlantic Ridge; SB, Scandinavian Blocking; IL, Icelandic Low.**

	NAO+	NAO-	AR	SB	IL
Winter					
Concatenated simulations	26.8	23.0	24.8	25.4	
PI	40.2	17.6	23.1	19.1	
MH$_{PMIP}$	26.7	23.1	25.7	24.4	
MH$_{GS}$	13.4	28.3	27.5	30.8	
Summer					
Concatenated simulations	28.3	25.4	18.5		27.8
PI	20.7	21.8	25.5		32.1
MH$_{PMIP}$	27.7	27.3	17.9		27.1
MH$_{GS}$	36.4	27.2	12.1		24.3
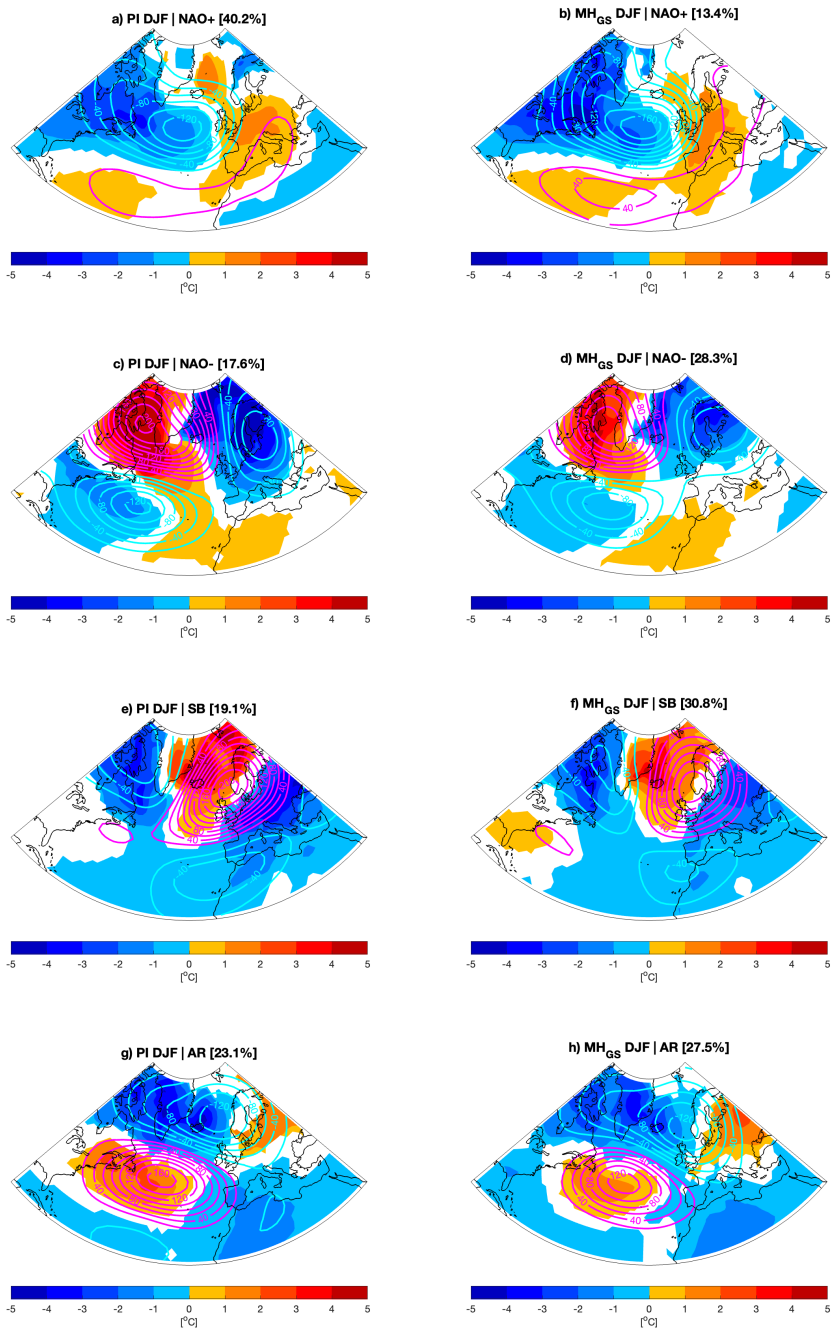
Figure 10. Winter North Atlantic WRs and associated thermal anomalies, respectively defined as the anomalies of the geopotential height at 500 hPa [m] and the 2-m temperature with respect to the climatology, in the (left) PI and (right) MH$_{GS}$ simulations. Only significant anomalies in 2-m temperature are shown, assessed by using a Student's *t* test at 95% confidence level.
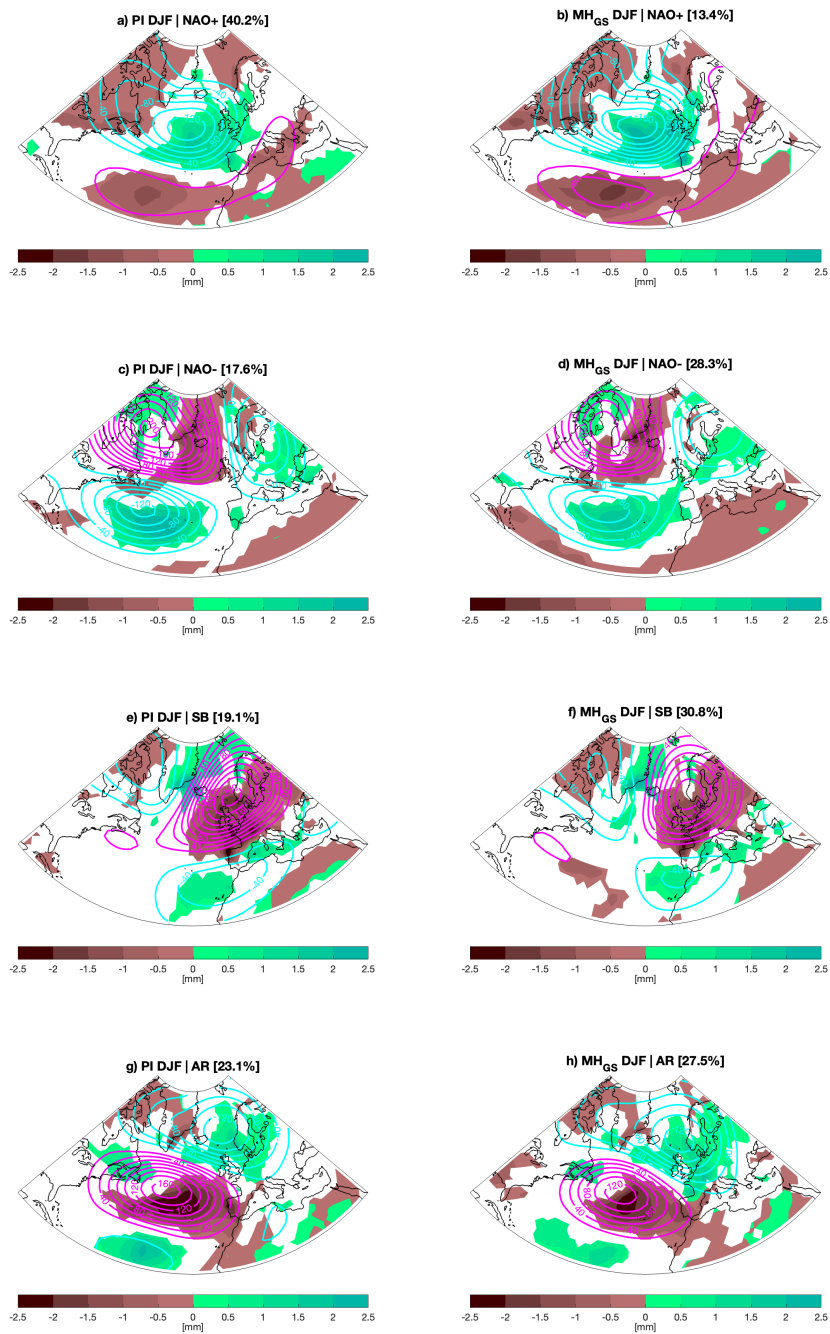
Figure 11. Winter North Atlantic WRs and associated rainfall anomalies, respectively defined as the anomalies of the geopotential height at 500 hPa [m] and daily precipitation with respect to the climatology, in the (left) PI and (right) MH$_{GS}$ simulations. Only significant anomalies in precipitation are shown, assessed by using a Student's *t* test at 95% confidence level.

Consistent with the literature, the summer synoptic circulation simulated by EC-Earth3.1 is characterised by NAO+, NAO-, AR and the Icelandic low (IL) (Cassou et al., 2005) **(Fig. A4)**. The NAO+, NAO- and IL show similar frequencies, characterising the atmospheric circulation in more than 80% of the analysed daily fields, while the occurrence of AR is much lower **(Table 2)**. Notably, the summer NAO+ and NAO- do not display symmetrically opposite circulation, as seen in the NAO's positive and negative phases defined as the first EOF of the interannual variability (see **Fig. A2b and A4a, b**). The modification of the orbital parameters in the MH experiments leads to an increased occurrence of both NAO+ and NAO- with respect to PI, along with a decrease in the IL and AR frequencies, making the NAO the dominant pattern of the synoptic variability in the MH$_{GS}$ (63.6% of the analysed daily fields are associated with NAO WRs, **Table 2**). The discrepancy between the increased occurrence of both NAO+ and NAO- WRs and the shift towards a negative phase in the monthly NAO can be explained by the differences in the spatial patterns discussed above. While NAO- well matches the negative phase of the monthly NAO (see **Fig. A2b and A4a**), NAO+ does not display a symmetric counterpart, with the high-pressure centre of action shifted above the Scandinavian peninsula (see **Fig. A4b**). This discrepancy is more a matter of terminology than a physical inconsistency. The predominance of NAO+ and NAO- WRs results in warm anomalies affecting southern and northern Europe and eastern North America when the Saharan greening is prescribed **(Fig. 12b, d)**. Conversely, the precipitation anomalies associated to the WR shift towards a NAO-dominated circulation primarily affect Europe, with no significant impact on North America. Specifically, the NAO+ is associated with dry anomalies in Scandinavia and the eastern Mediterranean, while NAO- leads to dry anomalies in southern Europe and the Mediterranean, accompanied by wet anomalies in western Europe and southern Scandinavia **(Fig. 13b, d).**
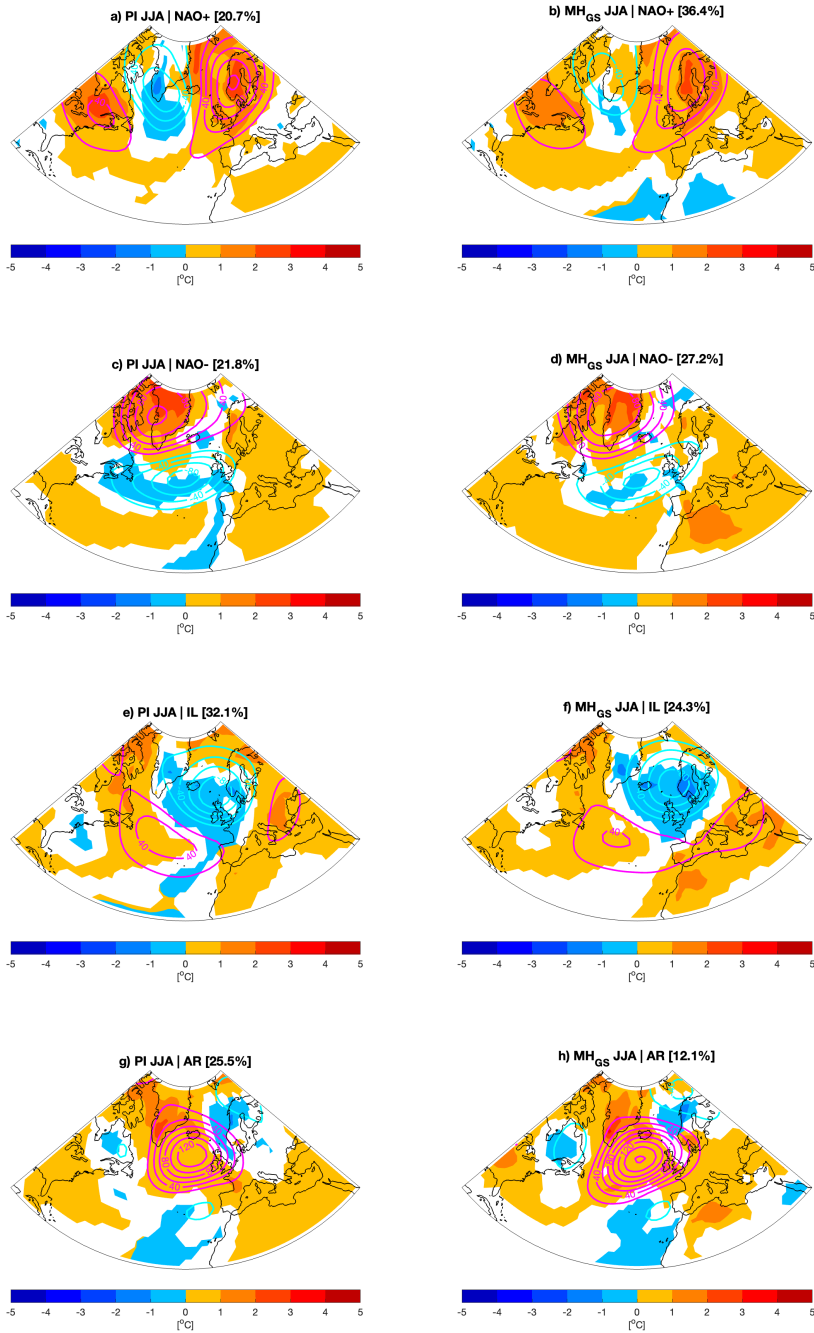
Figure 12. Summer North Atlantic WRs and associated thermal anomalies, respectively defined as the anomalies of the geopotential height at 500 hPa [m] and the 2-m temperature with respect to the climatology, in the (left) PI and (right) MH$_{GS}$ simulations. Only significant anomalies in 2-m temperature are shown, assessed by using a Student's *t* test at 95% confidence level.
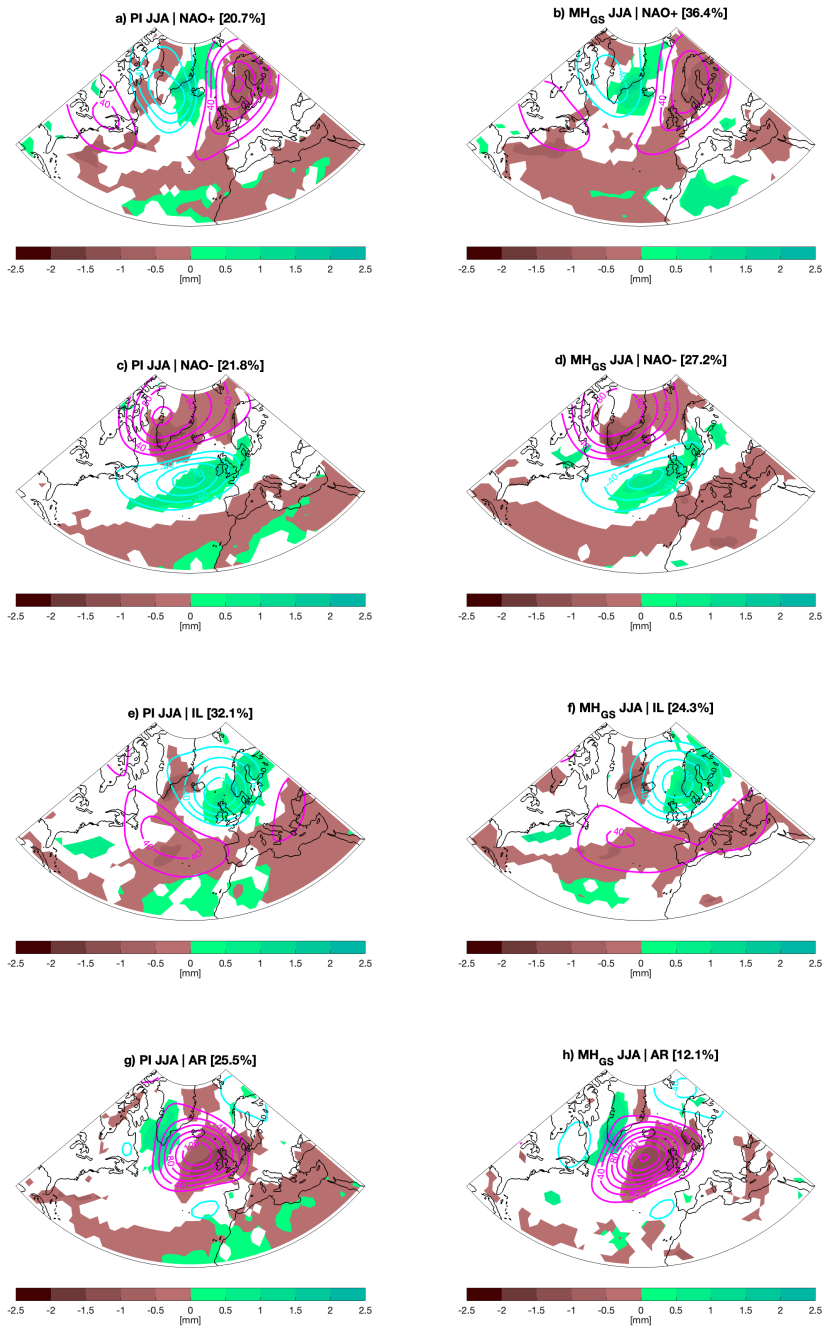
355

Figure 13. Summer North Atlantic WRs and associated rainfall anomalies, respectively defined as the anomalies of the geopotential height at 500 hPa [m] and daily precipitation with respect to the climatology, in the (left) PI and (right) MH$_{GS}$ simulations. Only significant anomalies in precipitation are shown, assessed by using a Student's *t* test at 95% confidence level.

4. Proxy-model comparison

The Cohen's Kappa index (κ) is used to quantify qualitative agreement between two datasets, with values ranging from -1 (complete disagreement) to 1 (perfect agreement). Here, the index indicates a generally low agreement between proxy reconstructions and model outputs over the mid-latitudes **(Table 3)**. Notably, the agreement for summertime temperatures is particularly low, with κ values very close to zero over all regions. For wintertime temperatures, κ values range from 0 to 0.158, indicating very low agreement except for the MH$_{PMIP}$ simulation over Asia (κ = 0.158). Annual precipitation shows slightly higher κ values, peaking at 0.28 for the MH$_{GS}$ simulation over Asia. In all cases but one (annual precipitation over Asia), the MH$_{PMIP}$ simulation shows higher κ values compared to the MH$_{GS}$ simulation.

A closer inspection of the proxy-model comparison reveals several factors contributing to the low agreement in summer temperatures. Firstly, the proxy reconstructions lack a spatial coherent large-scale pattern across the selected mid-latitude regions, with some coherence only found in some sub-regions, like Scandinavia. Secondly, both the MH$_{PMIP}$ and MH$_{GS}$ simulations indicate a strong mid-latitude warming signature, contrasting with the cooling shown in several reconstructions in North America and northern Asia. This suggests that the model may simulate an overly homogenous warming signal, while proxies indicate localised temperature increases. More importantly, the lack of coherent regional temperature signatures in the proxy reconstructions, suggest that low proxy-model agreement may not be exclusively due to model deficiencies. For annual precipitation, consistent regional signatures emerge over North America and Asia. North American proxies suggest a drier MH in the west and east, but wetter conditions in the southwest. While both MH$_{PMIP}$ and MH$_{GS}$ simulations capture the slight wettening in the southwest, they fail to simulate the drying reconstructed elsewhere. In Asia, a minor drying from ~45° E to ~100° E in the MH$_{PMIP}$ simulation is replaced by more extensive wettening in the MH$_{GS}$ simulation, leading to an improvement in the κ value for the region.

The overall low proxy-model agreement is further complicated by numerous inconclusive MH proxy records (as defined in Sec. 2, those record not providing a robust estimation of change or indicating no change) and the lack of consistent regional proxy signatures, except in specific sub-regions. This raises questions about the nature of MH climate anomalies: either the mid-latitudes lack coherent seasonal temperature patterns (unlike the tropics and high latitudes), suggesting limitations in the model's ability to capture regional climate nuances, or coherent climate signals do exist, and improvement in proxy-model agreements depend more on resolving discrepancies between proxies rather than solely on model improvements. In summary, the inclusion of vegetated Sahara in the model leads to improved agreement over Asia for precipitation and realistic representation of the drying in North America, albeit some spatial inaccuracies. This suggests that the MH$_{GS}$ simulation more effectively captures precipitation patterns compared to seasonal temperature patterns across the mid-latitudes.

Table 3. Cohen's Kappa index for region-wise proxy-model comparison, following DiNezio and Tierney (2013).

	Temperature (DJF)		Temperature (JJA)		Annual precipitation	
Region	MH$_{PMIP}$	MH$_{GS}$	MH$_{PMIP}$	MH$_{GS}$	MH$_{PMIP}$	MH$_{GS}$
North America: Pacific Coast	0.007	0.0	0.0	0.0	0.161	0.072
North America: Atlantic Coast	0.03	0.0	0.0	0.0	0.138	0.025
Western Europe and Mediterranean	0.003	0.0	0.0	0.0	0.021	0.002
Asia	0.158	0.072	0.0	0.0	0.205	0.28

5. Discussion and Conclusions

In this study, a set of atmosphere-ocean coupled climate model simulations are analysed to explore the impact of Saharan greening on mid-latitude atmospheric circulation and climate conditions in the Northern Hemisphere during the MH.
395 Specifically, two MH simulations are performed with and without prescribed vegetation cover and reduced dust emissions in the Sahara region, and compared to a PI control experiment. The climatological response in the Northern Hemisphere mid-latitudes is analysed, along with the modifications in the teleconnection patterns and the synoptic variability in the North Atlantic. To the authors' knowledge, this is the first study attempting to assess the MH climate modifications, including the Saharan greening, at mid-latitudes through the modelling of the atmospheric circulation variability at synoptic to interannual
400 time scales.

The MH experiments show significant changes in both surface temperature and precipitation in the mid-to-high latitudes with respect to the PI control simulation. The warming seen in the mid-to-high latitudes is attributed to increased summer insolation leading to decreased sea ice, with a sustained effect into winter, known as "summer remnant effect of insolation" (Yin and Berger, 2012). The increase in precipitation aligns with a significant reshaping of the large-scale circulation in the upper and
405 middle troposphere, including a westward shift of the global Walker Circulation and modifications in the westerly flow. Notably, these shifts result in altered surface climate in North America and Eurasia. The responses in temperature, precipitation and atmospheric dynamics are more pronounced in the MH$_{GS}$ simulation, indicating the significant influence of the Saharan greening on climate in the Northern Hemisphere. There is a broad literature on tropical-extratropical interactions triggered by tropical forcings such as the Indian monsoon and the El Niño/Southern Oscillation [e.g., Hoskins and Ambrizzi (1993);
410 Rodwell and Hoskins (1996)]. More recently, the African monsoon has been indicated as a possible source of tropical-extratropical teleconnections (Gaetani et al., 2011; Nakanishi et al., 2021), reinforcing the hypothesis that the strengthening of deep convection in northern Africa associated with the Saharan greening could lead to climate impacts in the extratropics. Moreover, the fact that the warm anomalies are more pronounced in MH$_{GS}$ than in MH$_{PMIP}$ simulation points to other drivers, beside the insolation, that could have amplified the warming. In particular, the prominent warming in the North Atlantic

415   simulated when vegetation is prescribed in the Sahara raises the possibility of modifications in the ocean circulation (see, e.g., Zhang et al. (2021), who found a strengthening of the Atlantic Meridional Overturning Circulation in response to the simulation of a green Sahara). Such changes could feasibly feedback on the atmosphere. Consequently, further studies focused on investigating potential changes in ocean circulation associated with the Saharan greening would be valuable for a better understanding of the widespread warming seen at mid-to-high latitudes.

420   The analysis of the interannual variability of the simulated mid-tropospheric circulation in the North Atlantic shows a significant shift from a prevailing positive NAO phase in the PI experiment to a prevailing neutral-to-negative phase in the MH experiments in both winter and summer. The impact is stronger when Saharan vegetation is prescribed, particularly in winter. The simulated changes in the NAO are in agreement with the existing literature (see e.g., Nesje et al., 2001; Rimbu et al., 2003; Olsen et al., 2012). However, although the simulated positive-to-negative shift of the monthly NAO is consistent

425   with the reconstructions of overall colder and dryer conditions in North America, it does not provide an explanation of the reconstructed thermal anomalies in Europe, especially regarding the warmer conditions in Scandinavia.

     In this respect, the analysis of the North Atlantic WR dynamics helps reconcile this discrepancy. The spatial patterns of the NAO WRs at the synoptic time scale, particularly the summer NAO+ and winter NAO-, display centres of action located over Scandinavia, differently from the interannual NAO patterns. In addition, it is shown that the simulated Saharan greening drives

430   modifications in the occurrence of other modes of the synoptic variability. The increased frequency of SB in winter and NAO+ in summer, both characterised by warm anomalies over Scandinavia, aligns with the warmer conditions found in the proxy records in the region and suggests a link to Saharan greening. The circulation anomalies associated with SB in winter and NAO+ in summer are consistent with those suggested by Mauri et al. (2014) to explain the MH thermal and precipitation anomalies in Northern Europe, namely stronger westerly and southerly flows towards Scandinavia in winter and summer.

435   The proxy-model comparison, while revealing limited agreement due to regional inconsistencies in proxy records, suggests that, where coherent climate reconstructions exist, the changes driven by the Saharan greening in the large-scale circulation indicate plausible explanations for the proxy evidence, especially for precipitation. This points to new opportunities for understanding the MH climate in the mid-latitudes. Furthermore, it should be noted that the simulation setup is highly idealised, initially tailored to enhance the representation of the MH precipitation in the Sahara and to improve the regional proxy-model

440   agreement. While this approach has yielded insights into specific climate impacts, such as those associated with Sahara greening, the broader applicability to global mid-Holocene climate scenarios is limited. The improvement of the global proxy-model agreement would benefit from more refined MH climate modelling strategies, such as prescribing more realistic vegetation across latitudes and considering the seasonal vegetation cycle (see e.g., Swann et al., 2014), which could better account for the nuanced large- and local-scale climate feedbacks that are critical for understanding past climates.

445

Appendix

Table A1. List of the locations, with coordinates, and references of the proxy records used for the quantification of the proxy-model agreement.

Site name	Latitude	Longitude	Original source
Annual precipitation			
Oro Lake, Canada	49.78	-105.33	Michels et al. (2007)
Ammersee	48	11.12	Czymzik et al. (2013)
Path Lake	43.87	-64.93	Neil et al. (2014)
Neor, Iran	37.96	48.56	Sharifi et al. (2015)
Lake Van	38.4	43.2	Chen et al. (2008)
Aral Sea	45	60	Chen et al. (2008)
Issyk-Kul	42.5	77.1	Chen et al. (2008)
Wulun Lake	47.2	87.29	Chen et al. (2008)
Bosten Lake	42	87.02	Chen et al. (2008)
Bayan Nuur	50	94.02	Chen et al. (2008)
Hovsgol Nuur	51	101.2	Chen et al. (2008)
Juyan Lake	41.8	101.8	Chen et al. (2008)
Gun Nuur	50.25	106.6	Chen et al. (2008)
Hulun Nuur	48.92	117.38	Chen et al. (2008)
Achit Nuur, Mongolia	49.42	90.52	Sun et al. (2013)
Oro Lake, Canada	49.78	-105.33	Michels et al. (2007)
Cleland Lake, British Columbia	50.83	-116.39	Steinman et al. (2016)
Paradise Lake, British Columbia	54.685	-122.617	Steinman et al. (2016)
Lime Lake, Washington	48.874	-117.338	Steinman et al. (2016)

Summer temperature			
Boothia Peninsula, Nunavut	69.9	-95.07	Zabenski and Gajewski (2017)
North Lake	69.24	-50.03	Axford et al. (2013)
Toskaljavri	69.2	21.47	Seppa et al. (2009)
KP2	68.8	35.32	Seppa et al. (2009)
Myrvatn	68.65	16.38	Seppa et al. (2009)
Austerkjosen	68.53	17.27	Seppa et al. (2009)
Yarnyshnoe	69.07	36.07	Seppa et al. (2008)
Lapland	69	25	Helama et al. (2012)
2005-804-004	68.99	-106.57	Ledu et al. (2010)
Liltlvatn	68.52	14.87	Seppa et al. (2008)
Gammelheimvatnet	68.47	17.75	Seppa et al. (2008)
Tsuolbmajavri	68.41	22.05	Seppa et al. (2008)
Lyadhej-To	68.25	65.79	Andreev et al. (2005)
Chuna	67.95	32.48	Solovieva et al. (2005)
Sjuuodjijaure	67.37	18.07	Rosén et al. (2001)
Kharinei	67.36	62.75	Jones et al. (2011)
MD95-2011	67	7.6	Calvo et al. (2002)
MD99-2269	66.85	-20.85	Justwan et al. (2008)
B997-321	66.53	-21.5	Smith et al. (2005)
Berkut	66.35	36.67	Ilyashuk et al. (2005)
Iglutalik	66.14	-66.08	Kerwin et al. (2004)
Screaming Lynx	66.07	-145.4	Clegg et al. (2011)
Honeymoon Pond	64.63	-138.4	Cwynar et al. (1991)

Svartvatnet	63.35	9.55	Seppa et al. (2009)
Tiavatnet	63.05	9.42	Seppa et al. (2009)
Kinnshaugen	62.02	10.37	Seppa et al. (2009)
Ratasjoen	62.27	9.83	Velle et al. (2005)
Hudson	61.9	-145.67	Clegg et al. (2011)
Haugtjern	60.83	10.88	Seppa et al. (2009)
Holebudalen	59.83	6.98	Seppa et al. (2009)
Brurskardstjorni	61.42	8.67	Velle et al. (2005)
Moose Lake	61.37	-143.6	Clegg et al. (2010)
Upper Fly Lake	61.07	-138.09	Bunbury and Gajewski (2009)
Trettetjorn	60.72	7	Bjune et al. (2005)
Rainbow	60.72	-150.8	Clegg et al. (2011)
s53s52	59.89	-104.21	Tillman et al. (2010)
Isbenttjonn	59.77	7.43	Seppa et al. (2009)
Flotatjonn	59.67	7.55	Seppa et al. (2009)
Grostjorn	58.53	7.73	Seppa et al. (2009)
Oykjamyrtjorn	59.82	6	Bjune et al. (2005)
LO09	58.94	-30.41	Berner et al. (2008)
K2	58.73	-65.93	Fallu et al. (2005)
Reiarsdalsvatnet	58.32	7.78	Seppa et al. (2009)
Dalene	58.25	8	Seppa et al. (2009)
Rice	48.01	-101.53	Shuman and Marsicek (2016)
Steel	46.97	-94.68	Shuman and Marsicek (2016)
Moon Lake	46.86	-98.16	Shuman and Marsicek (2016)

Pickerel	45.51	-97.27	Shuman and Marsicek (2016)
Nutt Lake	45.21	-79.45	Shuman and Marsicek (2016)
Graham Lake	45.19	-77.36	Shuman and Marsicek (2016)
Mansell	45.04	-68.73	Shuman and Marsicek (2016)
Sharkey	44.59	-93.41	Shuman and Marsicek (2016)
High Lake	44.52	-76.6	Shuman and Marsicek (2016)
Devils Lake	43.42	-89.73	Shuman and Marsicek (2016)
Okoboji Lake	43.37	-95.15	Shuman and Marsicek (2016)
Hams	43.24	-80.41	Shuman and Marsicek (2016)
Sutherland	41.39	-74.2	Shuman and Marsicek (2016)
Spruce Pond	41.24	-74.18	Shuman and Marsicek (2016)
Chatsworth	40.68	-88.34	Shuman and Marsicek (2016)
Hinterburgsee	46.72	8.07	Heiri et al. (2003)
Gemini Inferiore	44.39	10.05	Samartin et al. (2017)
Lago Verdarolo	44.36	10.12	Samartin et al. (2017)
Lago dell'Accesa	42.99	10.9	Finsinger et al. (2010)
Tagus Mud Patch	38.6	-9.5	Rodrigues et al. (2009)
Winter temperature			
Dalmutladdo	69.17	20.72	Bjune et al. (2004)
Candelabra	61.68	-130.65	Cwynar and Spear (1995)
Hail	60.03	-129.02	Cwynar and Spear (1995)
IOW225517	57.7	7.1	Emeis et al. (2003)
Lago dell'Accesa	42.99	10.9	Finsinger et al. (2010)
M25/4-KL11	36.7	17.7	Emeis et al. (2003)

450
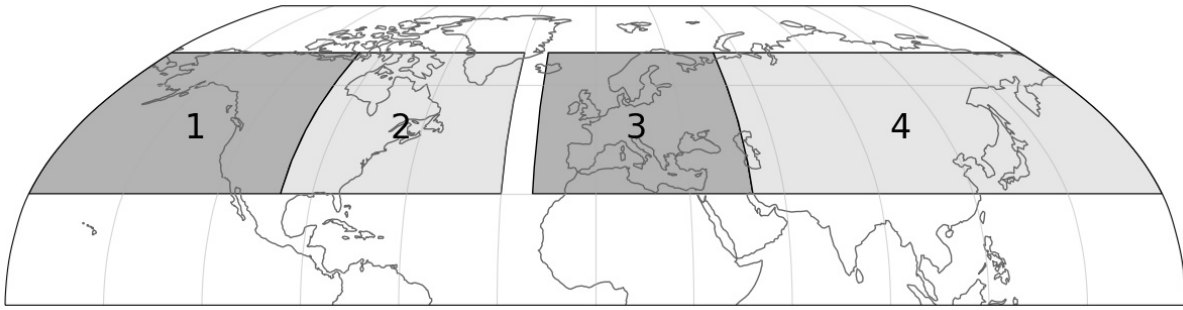
Figure A1. Regions used for Cohen's Kappa index calculations. From left to right: (1) North America, Pacific Coast (180–100°W, 30–70°N), (2) North America, Atlantic Coast (100–30°W; 30–70°N), (3) Europe and Mediterranean (20°W–50°E, 30–70°N), and (4) Asia (50–180°E, 30–70°N).

455
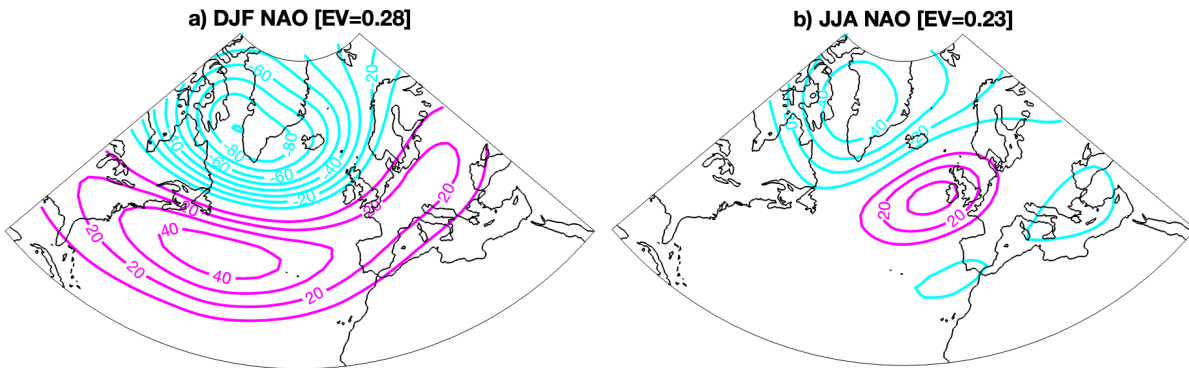
Figure A2. NAO anomaly patterns in (a) winter and (c) summer, obtained by regressing geopotential height at 500 hPa [m] onto the NAOI.
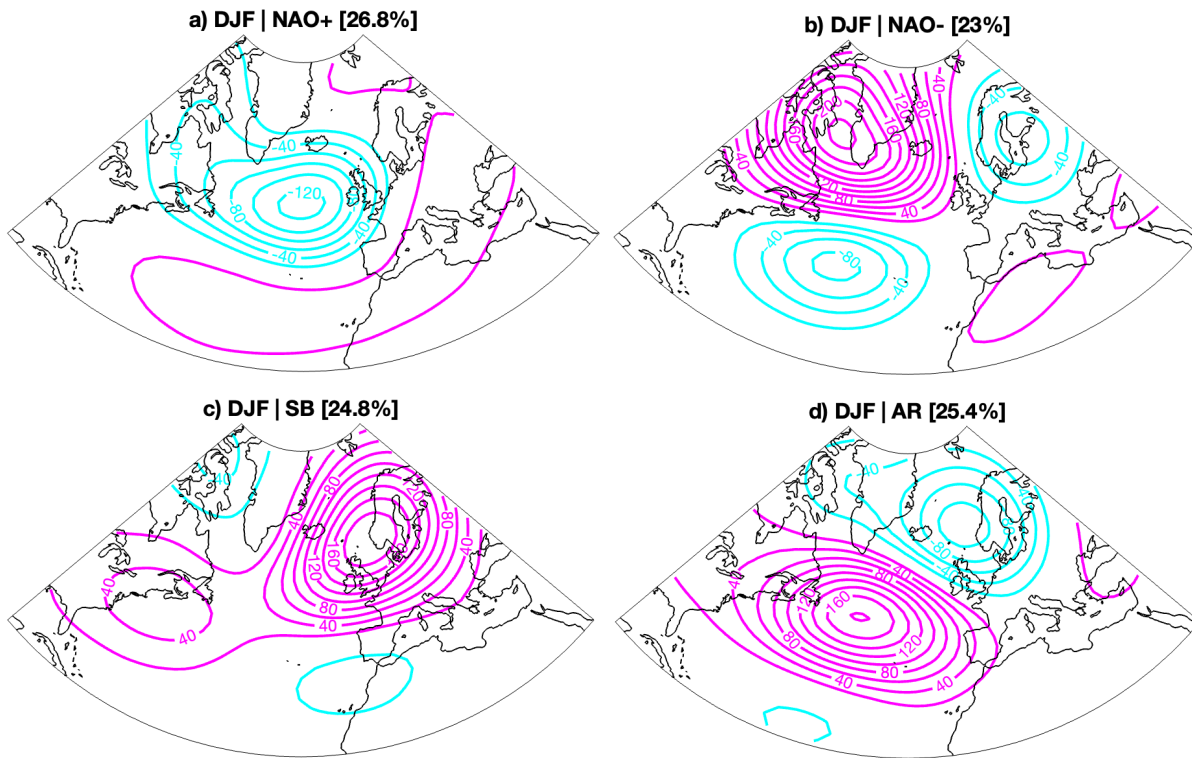
460

Figure A3. Winter North Atlantic WRs, defined as the anomalies of the geopotential height at 500 hPa [m] with respect to the climatology.
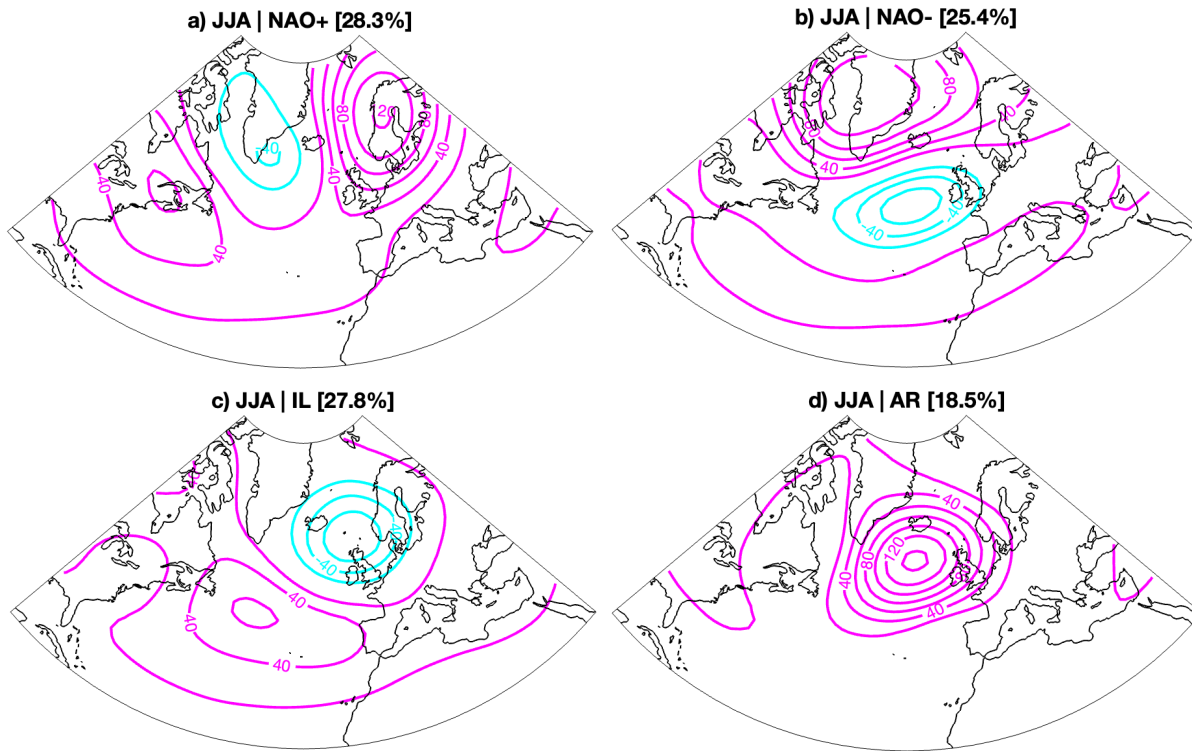
Figure A4. Summer North Atlantic WRs, defined as the anomalies of the geopotential height at 500 hPa [m] with respect to the climatology.

Code and data availability

All data and code are available upon request.

Author contribution

MG, GM and FSRP conceived the study. MG analysed the model simulations and wrote the paper. ST performed the proxy-model comparison and wrote the related section. MCAC and MG performed the WR classification. QZ ran the simulations. All the authors commented on the manuscript.

Competing interests

The authors declare that they have no conflict of interest

Acknowledgements

The authors thank S. Harrison for useful discussion, and two anonymous reviewers for their constructive comments. MG acknowledge the support of the project "Dipartimenti di Eccellenza 2023-2027", funded by the Italian Ministry of Education, University and Research at IUSS Pavia; and of the International Meteorological Institute based at the Department of Meteorology of Stockholm University. GM acknowledges the support of the Department of Earth Sciences of Uppsala University. FSRP and ST acknowledge the financial support from the Natural Sciences and Engineering Research Council of Canada (grant RGPIN-2018-04,981) and NSERC-FRQNT NOVA (grants ALLRP 577112-22 and 2023-NC-324826). QZ acknowledges the financial support from the Swedish Research Council (Vetenskapsrådet) (2017-04232, 2022-03617). The EC-Earth simulations and the data process were performed using ECMWF's computing and archive facilities and the National Academic Infrastructure for Supercomputing in Sweden (NAISS) and the Swedish National Infrastructure for Computing (SNIC) at NSC partially funded by the Swedish Research Council through grant agreements no. 2022-06725 and no. 2018-05973.

References

Adkins, J., deMenocal, P., and Eshel, G.: The "African humid period" and the record of marine upwelling from excess 230Th in Ocean Drilling Program Hole 658C, Paleoceanography, 21, 1–14, https://doi.org/10.1029/2005PA001200, 2006.

Ambaum, M. H. P., Hoskins, B. J., and Stephenson, D. B.: Arctic Oscillation or North Atlantic Oscillation?, J Clim, 14, 3495–3507, https://doi.org/10.1175/1520-0442(2001)014<3495:AOONAO>2.0.CO;2, 2001.

Andersson, C., Pausata, F. S. R., Jansen, E., Risebrobakken, B., and Telford, R. J.: Holocene trends in the foraminifer record from the Norwegian Sea and the North Atlantic Ocean, Climate of the Past, 6, 179–193, https://doi.org/10.5194/cp-6-179-2010, 2010.

Andreev, A. A., Tarasov, P. A., Ilyashuk, B. P., Ilyashuk E. A., Cremer, H., Hermichen, W.-D., Wischer, F., Hubberten, H.-W.: Holocene environmental history recorded in Lake Lyadhej-To sediments, Polar Urals, Russia, Palaeogeography, Palaeoclimatology, Palaeoecology, 223, 181-203, https://doi.org/10.1016/j.palaeo.2005.04.004, 2005.

Axford, Y., Losee, S., Briner, J. P., Francis, D. R., Langdon, P. G., and Walker, I. R.: Holocene temperature history at the western Greenland Ice Sheet margin reconstructed from lake sediments, Quat. Sci. Rev., 59, 87–100. https://doi.org/10.1016/j.quascirev.2012.10.024, 2013.

Bartlein, P. J., Harrison, S. P., Brewer, S., Connor, S., Davis, B. A. S., Gajewski, K., Guiot, J., Harrison-Prentice, T. I., Henderson, A., Peyron, O., Prentice, I. C., Scholze, M., Seppä, H., Shuman, B., Sugita, S., Thompson, R. S., Viau, A. E., Williams, J., and Wu, H.: Pollen-based continental climate reconstructions at 6 and 21 ka: A global synthesis, Clim Dyn, 37, 775–802, https://doi.org/10.1007/s00382-010-0904-1, 2011.

Bartlein, P. J., Harrison, S. P., and Izumi, K.: Underlying causes of Eurasian midcontinental aridity in simulations of mid-Holocene climate, Geophys Res Lett, 44, 9020–9028, https://doi.org/10.1002/2017GL074476, 2017.

Berner, K. S., Koç, N., Divine, D., Godtliebsen, F., and Moros, M.: A decadal-scale Holocene sea surface temperature record from the subpolar North Atlantic constructed using diatoms and statistics and its relation to other climate parameters, Paleoceanography, 23, PA2210, 2008.

Bjune, A. E., Bakke, J., Nesje, A., and Birks, H. J. B.: Holocene mean July temperature and winter precipitation in western Norway inferred from palynological and glaciological lake-sediment proxies, Holocene, 15, 177–189, 2005.

Bjune, A., Birks, H. J. B., and Seppä, H.: Holocene vegetation and climate history on a continental-oceanic transect in northern Fennoscandia based on pollen and plant macrofossils, Boreas, 33, 211–223, 2004.

Bladé, I., Liebmann, B., Fortuny, D., and van Oldenborgh, G. J.: Observed and simulated impacts of the summer NAO in Europe: Implications for projected drying in the Mediterranean region, Clim Dyn, 39, 709–727, https://doi.org/10.1007/s00382-011-1195-x, 2012.

Bosmans, J. H. C., Drijfhout, S. S., Tuenter, E., Lourens, L. J., Hilgen, F. J., and Weber, S. L.: Monsoonal response to mid-holocene orbital forcing in a high resolution GCM, Climate of the Past, 8, 723–740, https://doi.org/10.5194/cp-8-723-2012, 2012.

Bunbury, J., and Gajewski, K.: Postglacial climates inferred from a lake at treeline, southwest Yukon Territory, Canada, Quat. Sci. Rev., 28, 354–369, 2009.

Calvo, E., Grimalt, J., and Jansen, E.: High resolution U37K sea surface temperature reconstruction in the Norwegian Sea during the Holocene, Quat. Sci. Rev., 21, 1385–1394, 2002.

Cartapanis, O., Jonkers, L., Moffa-Sanchez, P., Jaccard, S. L., and de Vernal, A.: Complex spatio-temporal structure of the Holocene Thermal Maximum, Nat Commun, 13, 5662, https://doi.org/10.1038/s41467-022-33362-1, 2022.

Cassou, C., Terray, L., Hurrell, J. W., and Deser, C.: North Atlantic Winter Climate Regimes: Spatial Asymmetry, Stationarity with Time, and Oceanic Forcing, J Clim, 17, 1055–1068, https://doi.org/10.1175/1520-0442(2004)017<1055:NAWCRS>2.0.CO;2, 2004.

Cassou, C., Terray, L., and Phillips, A. S.: Tropical Atlantic influence on European heat waves, J Clim, 18, 2805–2811, https://doi.org/10.1175/JCLI3506.1, 2005.

Chandan, D. and Peltier, W. R.: African Humid Period Precipitation Sustained by Robust Vegetation, Soil, and Lake Feedbacks, Geophys Res Lett, 47, https://doi.org/10.1029/2020GL088728, 2020.

Chartrand, J. and Pausata, F. S. R.: Impacts of the North Atlantic Oscillation on winter precipitations and storm track variability in southeast Canada and the northeast United States, Weather and Climate Dynamics, 1, 731–744, https://doi.org/10.5194/wcd-1-731-2020, 2020.

Chen, F., Yu, Z., Yang, M., Ito, E., Wang, S., Madsen, D. B., Huang, X., Zhao, Y., Sato, T., Birks, H. J. B., Boomer, I., Chen, J., An, C., and Wünnemann, B.: Holocene moisture evolution in arid central Asia and its out-of-phase relationship with Asian monsoon history, Quat. Sci. Rev., 27, 351–364, 2008. https://doi.org/10.1016/j.quascirev.2007.10.017.

Claussen, M. and Gayler, V.: The Greening of the Sahara during the Mid-Holocene: Results of an Interactive Atmosphere-Biome Model, Global Ecology and Biogeography Letters, 6, 369-377, 1997.

Claussen, M., Kubatzki, C., Brovkin, V., Ganopolski, A., Hoelzmann, P., and Pachur, H.-J.: Simulation of an abrupt change in Saharan vegetation in the Mid-Holocene, Geophys Res Lett, 26, 2037–2040, https://doi.org/10.1029/1999GL900494, 1999.

Claussen, M., Dallmeyer, A., and Bader, J.: Theory and modeling of the African humid period and the green Sahara, in: Oxford Research Encyclopedia of Climate Science, Oxford University Press, 2017. https://doi.org/10.1093/acrefore/9780190228620.013.532.

Cronin, T. M., Thunell, R., Dwyer, G. S., Saenger, C., Mann, M. E., Vann, C., and Seal, I. R.: Multiproxy evidence of Holocene climate variability from estuarine sediments, eastern North America, Paleoceanography, 20, https://doi.org/10.1029/2005PA001145, 2005.

Clegg, B. F., Clarke, G. H., Chipman, M. L., Chou, M., Walker, I. R., Tinner, W., and Hu, F. S.: Six millennia of summer temperature variation based on midge analysis of lake sediments from Alaska, Quat. Sci. Rev., 29, 3308–3316, 2010. https://doi.org/10.1016/j.quascirev.2010.08.001.

Clegg, B. F., Kelly, R., Clarke, G. H., Walker, I. R., and Hu, F. S.: Nonlinear response of summer temperature to Holocene insolation forcing in Alaska, Proc. Natl. Acad. Sci. USA, 108, 19299–19304, 2011.

Cwynar, L. C., and Spear, R. W.: Paleovegetation and paleoclimatic changes in the Yukon at 6 ka BP, Géogr. Phys. Quat., 49, 29–35, 1995.

Cwynar, L. C., and Spear, R. W.: Reversion of forest to tundra in the central Yukon, Ecology, 72, 202–212, 1991.

Czymzik, M., Brauer, A., Dulski, P., Plessen, B., Naumann, R., von Grafenstein, U., and Scheffler, R.: Orbital and solar forcing of shifts in Mid- to Late Holocene flood intensity from varved sediments of pre-alpine Lake Ammersee (southern Germany), Quat. Sci. Rev., 61, 96–110, 2013. https://doi.org/10.1016/j.quascirev.2012.11.010.

Davis, B. A. S., Brewer, S., Stevenson, A. C., and Guiot, J.: The temperature of Europe during the Holocene reconstructed from pollen data, Quat Sci Rev, 22, 1701–1716, https://doi.org/10.1016/S0277-3791(03)00173-2, 2003.

deMenocal, P., Ortiz, J., Guilderson, T., Adkins, J., Sarnthein, M., Baker, L., and Yarusinsky, M.: Abrupt onset and termination of the African Humid Period: rapid climate responses to gradual insolation forcing, Quat Sci Rev, 19, 347–361, https://doi.org/https://doi.org/10.1016/S0277-3791(99)00081-5, 2000.

DiNezio, P. N. and Tierney, J. E.: The effect of sea level on glacial Indo-Pacific climate, Nat Geosci, 6, 485–491, https://doi.org/10.1038/ngeo1823, 2013.

Emeis, K.-C., Struck, U., Blanz, T., Kohly, A., and Voß, M.: Salinity changes in the central Baltic Sea (NW Europe) over the last 10,000 years, Holocene, 13, 411–421, 2003.

Fallu, M.-A., Pienitz, R., Walker, I. R., and Lavoie, M.: Paleolimnology of a shrub-tundra lake and response of aquatic and terrestrial indicators to climatic change in arctic Québec, Canada, Palaeogeogr. Palaeoclimatol. Palaeoecol., 215, 183–203, 2005.

Finsinger, W., Tinner, W., Conedera, M., and Ammann, B.: Early to mid-Holocene climate change at Lago dell'Accesa (central Italy): climate signal or anthropogenic bias?, J. Quat. Sci., 25, 1239–1247, 2010.

Folland, C. K., Knight, J., Linderholm, H. W., Fereday, D., Ineson, S., and Hurrell, J. W.: The Summer North Atlantic Oscillation: Past, Present, and Future, J Clim, 22, 1082–1103, https://doi.org/10.1175/2008JCLI2459.1, 2009.

Gaetani, M., Pohl, B., Douville, H., and Fontaine, B.: West African Monsoon influence on the summer Euro-Atlantic circulation, Geophys Res Lett, 38, 2011GL047150, https://doi.org/10.1029/2011GL047150, 2011.

Gaetani, M., Messori, G., Zhang, Q., Flamant, C., and Pausata, F. S. R.: Understanding the mechanisms behind the northward extension of the West African monsoon during the mid-holocene, J Clim, 30, 7621–7642, https://doi.org/10.1175/JCLI-D-16-0299.1, 2017.

Grams, C. M., Beerli, R., Pfenninger, S., Staffell, I., and Wernli, H.: Balancing Europe's wind-power output through spatial deployment informed by weather regimes, Nat Clim Chang, 7, 557–562, https://doi.org/10.1038/nclimate3338, 2017.

Harrison, S. P., Bartlein, P. J., Brewer, S., Prentice, I. C., Boyd, M., Hessler, I., Holmgren, K., Izumi, K., and Willis, K.: Climate model benchmarking with glacial and mid-Holocene climates, Clim Dyn, 43, 671–688, https://doi.org/10.1007/s00382-013-1922-6, 2014.

Haug, G. H., Hughen, K. A., Sigman, D. M., Peterson, L. C., and Röhl, U.: Southward Migration of the Intertropical Convergence Zone Through the Holocene, Science (1979), 293, 1304–1308, https://doi.org/10.1126/science.1059725, 2001.

Hazeleger, W., Severijns, C., Semmler, T., Ştefănescu, S., Yang, S., Wang, X., Wyser, K., Dutra, E., Baldasano, J. M., Bintanja, R., Bougeault, P., Caballero, R., Ekman, A. M. L., Christensen, J. H., van den Hurk, B., Jimenez, P., Jones, C., Kållberg, P., Koenigk, T., McGrath, R., Miranda, P., van Noije, T., Palmer, T., Parodi, J. A., Schmith, T., Selten, F., Storelvmo, T., Sterl, A., Tapamo, H., Vancoppenolle, M., Viterbo, P., and Willén, U.: EC-Earth, A Seamless earth-System Prediction Approach in Action, Bull Am Meteorol Soc, 91, 1357–1364, https://doi.org/10.1175/2010BAMS2877.1, 2010.

Heiri, O., Lotter, A. F., Hausmann, S., and Kienast, F.: A chironomid-based Holocene summer air temperature reconstruction from the Swiss Alps, Holocene, 13, 477–484, 2003.

600 Helama, S., Seppä, H., Bjune, A. E., and Birks, H. J. B.: Fusing pollen-stratigraphic and dendroclimatic proxy data to reconstruct summer temperature variability during the past 7.5 ka in subarctic Fennoscandia, J. Paleolimnol., 48, 275–286, 2012.

Hély, C., Lézine, A. M., Ballouche, A., Cour, P., Duzer, D., Guinet, P., Jahns, S., Maley, J., Mercuri, A. M., Pons, A., Ritchie, J. C., Salzmann, U., Schulz, E., Van Campo, M., and Waller, M. P.: Holocene changes in African vegetation: Tradeoff between 605 climate and water availability, Climate of the Past, 10, 681–686, https://doi.org/10.5194/cp-10-681-2014, 2014.

Hermann, N. W., Oster, J. L., and Ibarra, D. E.: Spatial patterns and driving mechanisms of mid-Holocene hydroclimate in western North America: Mid-Holocene Hydroclimate In Western North America, J. Quaternary Sci., 33, 421–434, https://doi.org/10.1002/jqs.3023, 2018.

Hochman, A., Messori, G., Quinting, J. F., Pinto, J. G., and Grams, C. M.: Do Atlantic-European Weather Regimes Physically 610 Exist?, Geophys Res Lett, 48, 1–10, https://doi.org/10.1029/2021GL095574, 2021.

Hoelzmann, P., Jolly, D., Harrison, S. P., Laarif, F., Bonnefille, R., and Pachur, H.-J.: Mid-Holocene land-surface conditions in northern Africa and the Arabian Peninsula: A data set for the analysis of biogeophysical feedbacks in the climate system, Global Biogeochem Cycles, 12, 35–51, https://doi.org/10.1029/97GB02733, 1998.

Hopcroft, P. O. and Valdes, P. J.: On the Role of Dust-Climate Feedbacks During the Mid-Holocene, Geophys Res Lett, 46, 615 1612–1621, https://doi.org/10.1029/2018GL080483, 2019.

Hoskins, B. J. and Ambrizzi, T.: Rossby Wave Propagation on a Realistic Longitudinally Varying Flow, J Atmos Sci, 50, 1661–1671, https://doi.org/10.1175/1520-0469(1993)050<1661:RWPOAR>2.0.CO;2, 1993.

Hurrell, J. W., Kushnir, Y., Ottersen, G., and Visbeck, M.: An overview of the North Atlantic Oscillation, in: Geophysical Monograph Series, vol. 134, 1–35, https://doi.org/10.1029/134GM01, 2003.

620 Ilyashuk, E. A., Ilyashuk, B. P., Hammarlund, D., and Larocque, I.: Holocene climatic and environmental changes inferred from midge records (Diptera: Chironomidae, Chaoboridae, Ceratopogonidae) at Lake Berkut, southern Kola Peninsula, Russia, Holocene, 15, 897–914, 2005.

Jiang, D., Tian, Z., and Lang, X.: Mid-Holocene global monsoon area and precipitation from PMIP simulations, Clim Dyn, 44, 2493–2512, https://doi.org/10.1007/s00382-014-2175-8, 2015.

625 Jones, V. J., Solovieva, N., Self, A. E., et al.: The influence of Holocene tree-line advance and retreat on an arctic lake ecosystem: a multi-proxy study from Kharinei Lake, North Eastern European Russia, J. Paleolimnol., 46, 123–137, 2011. https://doi.org/10.1007/s10933-011-9528-7.

Justwan, A., Koç, N., and Jennings, A. E.: Evolution of the Irminger and East Icelandic Current systems through the Holocene, revealed by diatom-based sea surface temperature reconstructions, Quat. Sci. Rev., 27, 1571–1582, 2008.

630 Kaufman, D. S., Ager, T. A., Anderson, N. J., Anderson, P. M., Andrews, J. T., Bartlein, P. J., Brubaker, L. B., Coats, L. L., Cwynar, L. C., Duvall, M. L., Dyke, A. S., Edwards, M. E., Eisner, W. R., Gajewski, K., Geirsdóttir, A., Hu, F. S., Jennings, A. E., Kaplan, M. R., Kerwin, M. W., Lozhkin, A. V., MacDonald, G. M., Miller, G. H., Mock, C. J., Oswald, W. W., Otto-Bliesner, B. L., Porinchu, D. F., Rühland, K., Smol, J. P., Steig, E. J., and Wolfe, B. B.: Holocene thermal maximum in the western Arctic (0-180°W), Quat Sci Rev, 23, 529–560, https://doi.org/10.1016/j.quascirev.2003.09.007, 2004.

635 Kaislahti Tillman, P., Holzkämper, S., Kuhry, P., Sannel, A. B. K., Loader, N. J., Robertson, I., Long-term climate variability in continental subarctic Canada: A 6200-year record derived from stable isotopes in peat, Palaeogeogr. Palaeoclimatol. Palaeoecol., 298, 235–246, 2010. https://doi.org/10.1016/j.palaeo.2010.09.029.

Kerwin, M. W., Overpeck, J. T., Webb, R. S., and Anderson, K. H.: Pollen-based summer temperature reconstructions for the eastern Canadian boreal forest, subarctic, and Arctic, Quat. Sci. Rev., 23, 1901–1924, 2004.

640 Larrasoaña, J. C., Roberts, A. P., and Rohling, E. J.: Dynamics of Green Sahara Periods and Their Role in Hominin Evolution, PLoS One, 8, e76514, https://doi.org/10.1371/journal.pone.0076514, 2013.

Ledu, D., Rochon, A., de Vernal, A., and St-Onge, G.: Holocene paleoceanography of the northwest passage, Canadian Arctic Archipelago, Quat. Sci. Rev., 29, 3468–3488, 2010.

Lézine, A.-M., Hély, C., Grenier, C., Braconnot, P., and Krinner, G.: Sahara and Sahel vulnerability to climate changes, lessons from Holocene hydrological data, Quat Sci Rev, 30, 3001–3012, https://doi.org/10.1016/j.quascirev.2011.07.006, 2011.

Madec, G., 2008: NEMO ocean engine. Note du Pole de modelisation 27, Institut Pierre-Simon Laplace, 396 pp.

Mauri, A., Davis, B. A. S., Collins, P. M., and Kaplan, J. O.: The influence of atmospheric circulation on the mid-Holocene climate of Europe: a data–model comparison, Clim. Past, 10, 1925–1938, https://doi.org/10.5194/cp-10-1925-2014, 2014.

McGee, D., DeMenocal, P. B., Winckler, G., Stuut, J. B. W., and Bradtmiller, L. I.: The magnitude, timing and abruptness of changes in North African dust deposition over the last 20,000yr, Earth Planet Sci Lett, 371–372, 163–176, https://doi.org/10.1016/j.epsl.2013.03.054, 2013.

Messori, G., Gaetani, M., Zhang, Q., Zhang, Q., and Pausata, F. S. R.: The water cycle of the mid-Holocene West African monsoon: The role of vegetation and dust emission changes, International Journal of Climatology, 39, 1927–1939, https://doi.org/10.1002/joc.5924, 2019.

Michelangeli, P. A., Vautard, R., and Legras, B.: Weather regimes: recurrence and quasi stationarity, https://doi.org/10.1175/1520-0469(1995)052<1237:WRRAQS>2.0.CO;2, 1995.

Michels, A., Laird, K. R., Wilson, S. E., Thomson, D., Leavitt, P. R., Oglesby, R. J., and Cumming, B. F.: Multidecadal to millennial-scale shifts in drought conditions on the Canadian prairies over the past six millennia: implications for future drought assessment, Global Change Biology, 13, 1295–1307, 2007. https://doi.org/10.1111/j.1365-2486.2007.01367.x.

Nakanishi, T., Tachibana, Y., and Ando, Y.: Possible semi-circumglobal teleconnection across Eurasia driven by deep convection over the Sahel, Clim Dyn, 57, 2287–2299, 2021. https://doi.org/10.1007/s00382-021-05804-x.

Neil, K., Gajewski, K., and Betts, M.: Human-ecosystem interactions in relation to Holocene environmental change in Port Joli Harbour, southwestern Nova Scotia, Canada, Quat. Res., 81, 2014.

Nesje, A., Matthews, J. A., Dahl, S. O., Berrisford, M. S., and Andersson, C.: Holocene glacier fluctuations of Flatebreen and winter-precipitation changes in the Jostedalsbreen region, western Norway, based on glaciolacustrine sediment records, Holocene, 11, 267–280, https://doi.org/10.1191/095968301669980885, 2001.

Olsen, J., Anderson, N. J., and Knudsen, M. F.: Variability of the North Atlantic Oscillation over the past 5,200 years, Nat Geosci, 5, 808–812, https://doi.org/10.1038/ngeo1589, 2012.

Pausata, F. S. R., Messori, G., and Zhang, Q.: Impacts of dust reduction on the northward expansion of the African monsoon during the Green Sahara period, Earth Planet Sci Lett, 434, 298–307, https://doi.org/10.1016/j.epsl.2015.11.049, 2016.

Pausata, F. S. R., Zhang, Q., Muschitiello, F., Lu, Z., Chafik, L., Niedermeyer, E. M., Stager, J. C., Cobb, K. M., and Liu, Z.: Greening of the Sahara suppressed ENSO activity during the mid-Holocene, Nat Commun, 8, https://doi.org/10.1038/ncomms16020, 2017a.

Pausata, F. S. R., Emanuel, K. A., Chiacchio, M., Diro, G. T., Zhang, Q., Sushama, L., Stager, J. C., and Donnelly, J. P.: Tropical cyclone activity enhanced by Sahara greening and reduced dust emissions during the African Humid Period, Proc Natl Acad Sci U S A, 114, 6221–6226, https://doi.org/10.1073/pnas.1619111114, 2017b.

Pausata, F. S. R., Gaetani, M., Messori, G., Berg, A., Maia de Souza, D., Sage, R. F., and DeMenocal, P. B.: The Greening of the Sahara: Past Changes and Future Implications, One Earth, 2, 235–250, https://doi.org/10.1016/j.oneear.2020.03.002, 2020.

Renssen, H., Seppä, H., Heiri, O., Roche, D. M., Goosse, H., and Fichefet, T.: The spatial and temporal complexity of the Holocene thermal maximum, Nat Geosci, 2, 411–414, https://doi.org/10.1038/ngeo513, 2009.

Rimbu, N., Lohmann, G., Kim, J.-H., Arz, H. W., and Schneider, R.: Arctic/North Atlantic Oscillation signature in Holocene sea surface temperature trends as obtained from alkenone data, Geophys Res Lett, 30, 2000–2003, https://doi.org/10.1029/2002GL016570, 2003.

Rodrigues, T., Grimalt, J. O., Abrantes, F. G., Flores, J. A., and Lebreiro, S. M.: Holocene interdependences of changes in sea surface temperature, productivity, and fluvial inputs in the Iberian continental shelf (Tagus mud patch), Geochem. Geophys. Geosystems, 10, Q07U06, 2009.

Rodwell, M. J., and Hoskins, B. J.: Monsoons and the dynamics of deserts, Quarterly Journal of the Royal Meteorological Society, 122, 1385–1404, 1996. https://doi.org/10.1256/smsqj.53407.

Rosén, P., Segerström, U., Eriksson, L., Renberg, I., and Birks, H. J. B.: Holocene climatic change reconstructed from diatoms, chironomids, pollen and near-infrared spectroscopy at an alpine lake (Sjuodjijaure) in northern Sweden, The Holocene, 11(5), 551-562, 2001. https://doi.org/10.1191/095968301680223503.

Sagoo, N. and Storelvmo, T.: Testing the sensitivity of past climates to the indirect effects of dust, Geophys Res Lett, 44, 5807–5817, https://doi.org/10.1002/2017GL072584, 2017.

Samartin, S., Heiri, O., Joos, F., Renssen, H., Franke, J., Brönnimann, S., and Tinner, W.: Warm Mediterranean mid-Holocene summers inferred from fossil midge assemblages, Nat Geosci, 10, 207–212, https://doi.org/10.1038/ngeo2891, 2017.

Scholz, D., Frisia, S., Borsato, A., Spötl, C., Fohlmeister, J., Mudelsee, M., Miorandi, R., and Mangini, A.: Holocene climate variability in north-eastern Italy: potential influence of the NAO and solar activity recorded by speleothem data, Climate of the Past, 8, 1367–1383, https://doi.org/10.5194/cp-8-1367-2012, 2012.

Seppä, H., Bjune, A. E., Telford, R. J., Birks, H. J. B., and Veski, S.: Last nine-thousand years of temperature variability in Northern Europe, Clim. Past, 5, 523–535, 2009.

Seppä, H., MacDonald, G. M., Birks, H. J. B., Gervais, B. R., and Snyder, J. A.: Late-Quaternary summer temperature changes in the northern-European tree-line region, Quat. Res., 69, 404–412, 2008.

Sharifi, A., Pourmand, A., Canuel, E. A., Ferer-Tyler, E., Peterson, L. C., Aichner, B., Feakins, S. J., Daryaee, T., Djamali, M., Naderi Beni, A., Lahijani, H. A. K., and Swart, P. K.: Abrupt climate variability since the last deglaciation based on a high-resolution, multi-proxy peat record from NW Iran: The hand that rocked the Cradle of Civilization?, Quat. Sci. Rev., 123, 215-230, 2015. https://doi.org/10.1016/j.quascirev.2015.07.006.

Shuman, B. N., and Marsicek, J.: The structure of Holocene climate change in mid-latitude North America, Quat. Sci. Rev., 141, 38–51, 2016.

Smith, L. M., Andrews, J. T., Castañeda, I. S., Kristjánsdóttir, G. B., Jennings, A. E., and Sveinbjörnsdóttir, Á. E.: Temperature reconstructions for SW and N Iceland waters over the last 10calka based on δ18O records from planktic and benthic Foraminifera, Quaternary Science Reviews, 24(14–15), 1723-1740, 2005. https://doi.org/10.1016/j.quascirev.2004.07.025.

Solovieva, N., Tarasov, P. E., and MacDonald, G.: Quantitative reconstruction of Holocene climate from the Chuna Lake pollen record, Kola Peninsula, northwest Russia, The Holocene, 15(1), 141-148, 2005. https://doi.org/10.1191/0959683605hl793rr.

Steinman, B. A., Pompeani, D. P., Abbott, M. B., Ortiz, J. D., Stansell, N. D., Finkenbinder, M. S., Mihindukulasooriya, L. N., and Hillman, A. L.: Oxygen isotope records of Holocene climate variability in the Pacific Northwest, Quaternary Science Reviews, 142, 40-60, 2016. https://doi.org/10.1016/j.quascirev.2016.04.012.

Sun, A., Feng, Z., Ran, M., and Zhang, C.: Pollen-recorded bioclimatic variations of the last ~22,600 years retrieved from Achit Nuur core in the western Mongolian Plateau, Quat. Int., 311, 36–43, 2013.

Sun, W., Wang, B., Zhang, Q., Pausata, F. S. R., Chen, D., Lu, G., Yan, M., Ning, L., and Liu, J.: Northern Hemisphere Land Monsoon Precipitation Increased by the Green Sahara During Middle Holocene, Geophys Res Lett, 46, 9870–9879, https://doi.org/10.1029/2019GL082116, 2019.

Swann, A. L. S., Fung, I. Y., and Chiang, J. C. H.: Mid-latitude afforestation shifts general circulation and tropical precipitation, Proceedings of the National Academy of Sciences, 109, 712–716, https://doi.org/10.1073/pnas.1116706108, 2012.

725 Swann, A. L. S., Fung, I. Y., Liu, Y., and Chiang, J. C. H.: Remote Vegetation Feedbacks and the Mid-Holocene Green Sahara, J Clim, 27, 4857–4870, https://doi.org/10.1175/JCLI-D-13-00690.1, 2014.

Taylor, K. E., Stouffer, R. J., and Meehl, G. A.: An Overview of CMIP5 and the Experiment Design, Bull Am Meteorol Soc, 93, 485–498, https://doi.org/10.1175/BAMS-D-11-00094.1, 2012.

Thompson, A. J., Skinner, C. B., Poulsen, C. J., and Zhu, J.: Modulation of Mid-Holocene African Rainfall by Dust Aerosol
730 Direct and Indirect Effects, Geophys Res Lett, 46, 3917–3926, https://doi.org/10.1029/2018GL081225, 2019.

Tierney, J. E. and DeMenocal, P. B.: Abrupt Shifts in Horn of Africa Hydroclimate Since the Last Glacial Maximum, Science (1979), 342, 843–846, https://doi.org/10.1126/science.1240411, 2013.

Tierney, J. E., Lewis, S. C., Cook, B. I., LeGrande, A. N., and Schmidt, G. A.: Model, proxy and isotopic perspectives on the East African Humid Period, Earth Planet Sci Lett, 307, 103–112, https://doi.org/10.1016/j.epsl.2011.04.038, 2011.

735 Tierney, J. E., Pausata, F. S. R., and DeMenocal, P. B.: Rainfall regimes of the Green Sahara, Sci Adv, 3, 1–9, https://doi.org/10.1126/sciadv.1601503, 2017.

Valcke, S., 2006: OASIS3 user guide. PRISM Tech. Rep. 3, 64 pp. [Available online at http://www.prism.enes.org/Publications/Reports/oasis3_UserGuide_T3.pdf.]

Vancoppenolle, M., Fichefet, T., Goosse, H., Bouillon, S., Madec, G., and Maqueda, M. A. M.: Simulating the mass balance
740 and salinity of Arctic and Antarctic sea ice. 1. Model description and validation, Ocean Model (Oxf), 27, 33–53, https://doi.org/10.1016/j.ocemod.2008.10.005, 2009.

van den Hurk BJJM, Viterbo P, Beljaars ACM, Betts AK (2000) Offline validation of the ERA40 surface scheme. ECMWF Tech Memo 295, 42 pp ECMWF, Reading.

Velle, G., Brooks, S. J., Birks, H. J. B., and Willassen, E.: Chironomids as a tool for inferring Holocene climate: an assessment
745 based on six sites in southern Scandinavia, Quat. Sci. Rev., 24, 1429–1462, 2005.

Wang, Y., Cheng, H., Edwards, R. L., Kong, X., Shao, X., Chen, S., Wu, J., Jiang, X., Wang, X., and An, Z.: Millennial- and orbital-scale changes in the East Asian monsoon over the past 224,000 years, Nature, 451, 1090–1093, https://doi.org/10.1038/nature06692, 2008.

Wilks, D. S.: Statistical Methods in the Atmospheric Sciences, Fourth Edition, 1–818 pp., https://doi.org/10.1016/C2017-0-
750 03921-6, 2019.

Wu, C.-H. and Tsai, P.-C.: Impact of orbitally-driven seasonal insolation changes on Afro-Asian summer monsoons through the Holocene, Commun Earth Environ, 2, 4, https://doi.org/10.1038/s43247-020-00073-8, 2021.

Yin, Q. Z. and Berger, A.: Individual contribution of insolation and CO2 to the interglacial climates of the past 800,000 years, Clim Dyn, 38, 709–724, https://doi.org/10.1007/s00382-011-1013-5, 2012.

755 Yuan, D., Cheng, H., Edwards, R. L., Dykoski, C. A., Kelly, M. J., Zhang, M., Qing, J., Lin, Y., Wang, Y., Wu, J., Dorale, J. A., An, Z., and Cai, Y.: Timing, Duration, and Transitions of the Last Interglacial Asian Monsoon, Science (1979), 304, 575–578, https://doi.org/10.1126/science.1091220, 2004.

Zabenskie, S., and Gajewski, K.: Post-Glacial climatic change on Boothia Peninsula, Nunavut, Canada, Quat. Res., 68, 261–270, 2007.

760 Zhang, M., Liu, Y., Zhang, J., and Wen, Q.: AMOC and Climate Responses to Dust Reduction and Greening of the Sahara during the Mid-Holocene, J Clim, 34, 4893–4912, https://doi.org/10.1175/JCLI-D-20-0628.1, 2021.

Zhao, Y. and Harrison, S. P.: Mid-Holocene monsoons: a multi-model analysis of the inter-hemispheric differences in the responses to orbital forcing and ocean feedbacks, Clim Dyn, 39, 1457–1487, https://doi.org/10.1007/s00382-011-1193-z, 2012.

765